JGR Atmospheres

RESEARCH ARTICLE
10.1029/2023JD039115

Modeling Wind-Blown Umbrella Clouds in Lagrangian Dispersion Models

F. J. Millward[1], **H. N. Webster**[2,3], **and C. G. Johnson**[1]

[1]Department of Mathematics, and Centre for Nonlinear Dynamics, University of Manchester, Manchester, UK, [2]Met Office, Devon, UK, [3]College of Engineering, Mathematics and Physical Sciences, University of Exeter, Devon, UK

Key Points:

- A non-axisymmetric parametrization of umbrella cloud spreading in wind is derived from a shallow-layer intrusion model
- The new parametrization describes buoyancy-driven spreading in both near-circular umbrella clouds and in strongly wind-blown plumes
- The predictions of a Volcanic Ash Transport and Dispersion Model are improved by the new parametrization, compared to axisymmetric models

Supporting Information:

Supporting Information may be found in the online version of this article.

Correspondence to:

C. G. Johnson,
chris.johnson@manchester.ac.uk

Citation:

Millward, F. J., Webster, H. N., & Johnson, C. G. (2023). Modeling wind-blown umbrella clouds in Lagrangian Dispersion Models. *Journal of Geophysical Research: Atmospheres*, *128*, e2023JD039115. https://doi.org/10.1029/2023JD039115

Received 20 APR 2023
Accepted 20 AUG 2023

Author Contributions:

Conceptualization: F. J. Millward, C. G. Johnson
Funding acquisition: C. G. Johnson
Investigation: F. J. Millward, C. G. Johnson
Methodology: F. J. Millward, H. N. Webster, C. G. Johnson
Software: F. J. Millward, H. N. Webster
Supervision: C. G. Johnson
Validation: F. J. Millward
Writing – original draft: F. J. Millward
Writing – review & editing: F. J. Millward, H. N. Webster, C. G. Johnson

Abstract The ash and gas released by large explosive volcanic eruptions rises to its neutral buoyancy level in the atmosphere, then spreads laterally to form an umbrella cloud. Density stratification of the atmosphere generates buoyancy forces in the cloud, which drive the outward spread. Although umbrella clouds are often modeled as circular axisymmetric structures, in practice they are usually influenced quite strongly by the meteorological wind, with spread in the upwind direction halted by the oncoming wind, and different rates of spreading in the downwind and crosswind directions. In this work, we derive a simple parametrization of non-axisymmetric umbrella cloud spreading from a much more complex physically based shallow-layer intrusion model. The new parametrization is quick to evaluate and so is suitable for use in operational Volcanic Ash Transport and Dispersion Models (VATDMs). In contrast to previous parametrizations, in which there is assumed to be no interaction between a circular umbrella cloud and the meteorological wind, here the umbrella cloud is influenced by the wind and adopts a shape determined by the balance of buoyant spreading and downwind drag forces. We apply the new scheme to four historical case studies of eruptions at Puyehue 2011, Pinatubo 1991, Ulawun 2019, and Calbuco 2015. The results are compared with VATDM simulations using a conventional circular umbrella cloud parametrization. Using the new scheme, good descriptions of cloud spread are recovered and the prediction of horizontal ash distribution is improved relative to the axisymmetric parametrization.

Plain Language Summary Erupting volcanoes eject a mixture of fine ash and gas, which rises into the upper atmosphere, where the ash presents a major hazard to jet aircraft. Large volcanic eruptions produce a giant cloud of ash, known as an umbrella cloud, which spreads horizontally. The spread of this umbrella cloud is driven by the variation in atmospheric density across its depth. Umbrella clouds are commonly assumed to be cylindrical, but in reality, they often assume a more complex shape, due to the influence of wind. In this paper, we derive a new mathematical model of umbrella cloud spreading that includes the effect of wind, which can be simulated on a computer quickly enough to produce practical forecasts of volcanic ash transport. The new model is applied to four historical eruptions and shown to produce good predictions of the umbrella cloud shape and extent in each case. Compared to existing cylindrical models, the distribution of ash inside the cloud is much improved.

1. Introduction

Explosive volcanic eruptions eject a mixture of hot volcanic gases and tephra at high vertical velocities. The fallout of larger tephra and entrainment of surrounding air during the explosive rise of the tephra-gas mix causes a convective plume of volcanic ash and gas to develop (Sparks, 1986). For larger, Plinian eruptions (those with volcanic explosivity index [VEI] ≥4, Newhall & Self, 1982), this plume rises up into the stratosphere until it reaches the level of neutral buoyancy (i.e., the height at which the density of the ash-gas mix is equal to that of the surrounding atmosphere). The plume continues to rise above this height due to excess vertical momentum, before the negative buoyancy of the overshooting plume causes it to collapse back to the neutral buoyancy level. The difference in vertical density gradient between the plume, which is relatively well mixed, and the surrounding atmosphere, which is stratified, induces horizontal pressure gradients in the ash-gas mix, driving its lateral spread along the neutral buoyancy level in a giant structure known as an umbrella cloud. Although this buoyancy spreading is most important close to the volcanic vent, it can be an important process in the lateral spreading of a plume hundreds of kilometers downwind from the volcano vent (Bursik, Carey, & Sparks, 1992; Johnson et al., 2015).

The spread of volcanic ash in the atmosphere is a serious concern for aviation, as encounters between jet aircraft and ash can cause engines to suffer accelerated wear or even shutdown (Clarkson et al., 2016). To mitigate these risks, aviation authorities impose restrictions on flight operations when ash is detected or, in Europe, when the concentration exceeds thresholds at 0.2, 2, and 4 mg/m^3 (International Civil Aviation Organization, 2021b). Together with ground-based and satellite observations, predictions by mathematical models are vital in identifying areas that violate these thresholds.

Around the world, Nine Volcanic Ash Advisory Centers (VAACs) use Volcanic Ash Transport and Dispersion Models (VATDMs) to predict the spread of atmospheric ash following an eruption. VAACs are required to rapidly produce forecasts of ash spread once notified of an eruption (International Civil Aviation Organization, 2017). These forecasts must then be regularly updated to reflect changing atmospheric conditions and variations in the intensity and mode of eruption. Consequently, VATDMs must be robust and computationally efficient.

VATDMs model ash transport due to advection by meteorological wind and other processes including gravitational settling and turbulent diffusion, but have historically neglected the buoyancy-driven spread of the ash. This may result in significant underprediction of the spread of ash from large Plinian (and ultra-Plinian) eruptions. Using the NAME (Numerical Atmospheric-dispersion Modeling Environment) VATDM to model the historic 1991 Pinatubo eruption, Witham et al. (2012) found that the spread of the cloud was substantially underestimated and attributed this in part to the absence of a parametrization of buoyancy spreading in the model. Witham et al. (2012) attempted to mitigate the effect of the missing buoyancy spreading by replacing the point ash source with a large elliptical source intended to represent the umbrella cloud, but found that the spread of the plume was still not accurately reproduced. Bonadonna et al. (2005) accurately simulated the buoyancy-driven crosswind spread of the 1996 Ruapehu eruption using a Fickian diffusion law. However, as Bonadonna et al. (2005) acknowledge, buoyancy-driven spreading is not a diffusion-like process and such an approach does not correctly describe the underlying physics. This is reflected in the size of the diffusion coefficient needed to reproduce the crosswind extent of the Ruapehu cloud, which is an order of magnitude larger than values typical for advection-diffusion models. Further, Bonadonna et al. (2005) noted that the appropriate diffusion coefficient will vary significantly between eruptions, making such an approach unsuitable for use in a predictive capacity.

More recently, improved predictions of ash spread have been obtained in VATDMs by including a parametrization of buoyancy-driven ash transport that is based on the axisymmetric umbrella cloud scaling of Woods and Kienle (1994). Woods and Kienle (1994) proposed that, for an umbrella cloud that remains circular and centered on the volcanic vent, the radius of the cloud R scales with time t as $R(t) \sim t^{2/3}$. To parametrize umbrella cloud spreading in the FALL3D VATDM, Costa et al. (2013) constructed an axisymmetric velocity field consistent with the cloud radius scaling of Woods and Kienle (1994) and summed it with the meteorological wind field used for passive advection. Variations on this approach, developed by Mastin et al. (2014) and Webster et al. (2020), have incorporated axisymmetric umbrella cloud parametrizations in the Ash3d (Schwaiger et al., 2012) and NAME (Jones et al., 2007) VATDMs. These axisymmetric parametrizations have been successfully applied to a range of historical case studies, including both the 1991 Pinatubo and 2015 Calbuco eruptions, which have been simulated using each of NAME (Webster et al., 2020), FALL3D (Costa et al., 2013; Folch et al., 2022) and Ash3d (Mastin & Van Eaton, 2020; Mastin et al., 2014).

A feature common to these parametrizations is that the umbrella cloud dynamics are based on the scaling for axisymmetric umbrella cloud radius originally proposed by Woods and Kienle (1994). Since then, considerable advances have been made in the study of umbrella clouds, with more recent modeling focused on solving the underlying partial differential equations (PDEs) that govern the motion of fluid in an umbrella cloud. These are the compressible Navier-Stokes equations, which can be solved directly to model the umbrella cloud (e.g., Suzuki & Koyaguchi, 2009), or depth-integrated into shallow-layer flow equations which model the cloud as an intrusion through a stratified atmosphere (Baines, 2013; de' Michieli Vitturi & Pardini, 2021; Johnson et al., 2015; Pouget et al., 2016; Ungarish & Huppert, 2002). The three principal benefits of such PDE-based models of umbrella clouds, over the Woods and Kienle (1994) axisymmetric cloud scaling are: (a) inclusion of the influence of wind, leading to a non-circular umbrella cloud, (b) a much more detailed prediction of the umbrella cloud properties, including the time- and space-dependent depth and internal velocity fields, and (c) greater physical justification, being solutions of the underlying equations of fluid mass and momentum conservation, rather than a scaling argument. However, the moderate to high computational cost of PDE-based models has made them less well suited for operational use in a VATDM, where very short run-times of only a few minutes are required.

In this paper, we present a new non-axisymmetric umbrella cloud parametrization based on the shallow-layer PDE model of Johnson et al. (2015). The parametrization is designed to maintain many of the benefits of a full PDE model, while being fast enough to evaluate that it is suitable for operational use within a VATDM. Like the model of Johnson et al. (2015) on which it is based, the new parametrization incorporates the effect of meteorological wind on the spread of the umbrella cloud, and the predicted umbrella cloud shape is therefore non-axisymmetric. Furthermore, the new parametrization provides umbrella cloud depth and velocity fields that satisfy both mass and momentum conservation equations, which we show cannot be achieved in parametrizations based on the Woods and Kienle scaling law. We test the new parametrization in the NAME VATDM, which is developed by the UK Met Office and used operationally by the London VAAC (Beckett et al., 2020), and compare the results to satellite observations and results of the axisymmetric parametrization of Webster et al. (2020) in four case-study eruptions: Puyehue 2011, Pinatubo 1991, Ulawun 2019, and Calbuco 2015.

In Section 2, we introduce the shallow-layer PDE umbrella cloud model of Johnson et al. (2015) (Section 2.1), and explain how existing axisymmetric umbrella cloud parametrizations can be seen as simplifications of this shallow-layer model (Section 2.2). We then derive the new non-axisymmetric parametrization presented in this paper (Section 2.3) and show how this may be used to modify model ash particle trajectories in the NAME VATDM (Section 2.4). In Section 3, we discuss the appropriate selection of model and eruption parameters, and test the new parametrization against satellite observations of eruptions at Puyehue, Pinatubo, Ulawun, and Calbuco, comparing with the previous axisymmetric model of Webster et al. (2020). In Section 4, we discuss the runtime of the new parametrization and methods of parameter estimation, and conclude in Section 5.

2. Modeling of Umbrella Clouds

2.1. The Shallow-Layer Model for Umbrella Clouds

The shallow-layer model of Johnson et al. (2015) is a general model for umbrella clouds, suitable for a wide range of initial and boundary conditions. For simplicity, we introduce it here as a model for an umbrella cloud supplied by a constant volume flux (at neutral buoyancy) Q, evolving in a steady uniform horizontal wind field $\mathbf{U} = (U, 0)$. The atmosphere is assumed to be stably stratified with constant buoyancy frequency N, and the umbrella cloud then spreads symmetrically about the level of neutral buoyancy $z = H_{\text{nbl}}$ as a cloud of total depth $h(x, y, t)$, which varies in both horizontal space and time. It is assumed that the depth of the cloud is much smaller than its horizontal extent, such that vertical velocities are small relative to horizontal velocities, and the vertical pressure balance inside the cloud is hydrostatic. Consequently, the motion of the intrusion may be described by the in-plane velocity field $\boldsymbol{u} = (u, v)$, a function of time t and the in-plane (horizontal) position $\boldsymbol{x} = (x, y)$ (with origin at the location of the volcano).

Under this set of assumptions, the depth and velocity of the cloud satisfy the system of PDEs (Johnson et al., 2015; Ungarish & Huppert, 2002),

$$\frac{\partial h}{\partial t} + \frac{\partial}{\partial x}(hu) + \frac{\partial}{\partial y}(hv) = q(\boldsymbol{x}), \tag{1a}$$

$$\frac{\partial}{\partial t}(hu) + \frac{\partial}{\partial x}\left(hu^2\right) + \frac{\partial}{\partial y}(huv) + \frac{\partial}{\partial x}\left(\frac{N^2h^3}{12}\right) = C_D(U-u)|\boldsymbol{U}-\boldsymbol{u}|, \tag{1b}$$

$$\frac{\partial}{\partial t}(hv) + \frac{\partial}{\partial x}(huv) + \frac{\partial}{\partial y}\left(hv^2\right) + \frac{\partial}{\partial y}\left(\frac{N^2h^3}{12}\right) = -C_D v|\boldsymbol{U}-\boldsymbol{u}|, \tag{1c}$$

where $q(\boldsymbol{x})$ is a source term representing the flux of volume into the umbrella cloud from the rising plume (which will be equal to zero except close to the origin). The total volume flux entering the cloud is

$$Q = \iint q(\boldsymbol{x})\, d\boldsymbol{x}. \tag{2}$$

These equations represent, respectively, the conservation of mass, and the conservation of momentum in the x- and y-directions. The first three terms in each component of the momentum balance, Equations 1b and 1c represent the inertia of the cloud, and the fourth represents pressure gradients caused by spatial variation in the cloud depth h. On the right hand side of the momentum equations, C_D is the coefficient of turbulent skin drag,

which describes the magnitude of the shear stress exerted on the upper and lower surfaces of the ash cloud by the atmosphere. These shear stresses arise from the instability of the cloud-atmosphere interface caused by the difference in velocity across the boundary (Abraham et al., 1979).

At the outer boundary of the cloud, atmospheric air must be vertically displaced for the cloud to spread horizontally along the neutral buoyancy layer, and the energy lost in this process slows the advance of the cloud (Ungarish, 2009). This energy loss is described by the Froude number front condition (Ungarish & Huppert, 2002) which relates the local spreading rate of the cloud to the cloud depth at the front by

$$\frac{2|(\boldsymbol{U}-\boldsymbol{u})\cdot\hat{\boldsymbol{n}}|}{Nh} = Fr_f. \tag{3}$$

The constant $\mathrm{Fr}_f \approx 0.841$ is the Froude number at the front of the current (Ungarish, 2009) and $\hat{\boldsymbol{n}} = (n_x, n_y)$ is an outward-oriented unit vector, normal to the cloud front.

2.2. Axisymmetric Parametrizations

The axisymmetric umbrella cloud parametrizations developed by Costa et al. (2013), Mastin et al. (2014), and Webster et al. (2020) are based on the $R \sim t^{2/3}$ scaling law for the radius of a cylindrical umbrella cloud in the absence of wind, proposed by Woods and Kienle (1994). These parametrizations model buoyancy spreading by advecting ash in a velocity field that is equal to the sum of meteorological wind and an axisymmetric velocity field consistent with the Woods and Kienle (1994) scaling law.

Woods and Kienle's modeling of the cylindrical umbrella cloud and the axisymmetric velocity field within it may be understood as simplifications of the full shallow-layer intrusion model described by Equations 1 and 3. We derive the cylindrical descriptions of spreading umbrella clouds used by Costa et al. (2013)'s and Webster et al. (2020)'s axisymmetric parametrizations in this context here, then discuss how two significant assumptions in the derivation lead to some associated shortcomings in the resulting models.

The first major assumption made in both derivations is that the atmosphere is stationary, such that $U = 0$. As a result of this assumption, buoyancy-driven spreading is completely decoupled from the meteorological wind in these parametrizations. Making this same assumption in the shallow-layer model, governing Equation 1 and the boundary condition (Equation 3) now imply the cloud will be axisymmetric, with a radius $R(t)$ and radial velocity $\boldsymbol{u} = u_r\boldsymbol{e}_r$ where $\boldsymbol{e}_r$ is a radial unit vector. The boundary condition (Equation 3), along with a kinematic condition relating the rate of expansion and front speed,

$$u_r|_{r=R(t)} = \frac{\mathrm{d}R}{\mathrm{d}t}, \tag{4}$$

implies that the cloud radius $R(t)$ must satisfy

$$\frac{\mathrm{d}R}{\mathrm{d}t} = \frac{Fr_f N}{2} h|_{r=R(t)}. \tag{5}$$

The second major assumption of Costa et al. (2013), Woods and Kienle (1994), and Webster et al. (2020) is that the depth of the umbrella cloud is uniform in space $h = h(t)$ (i.e., the cloud is a cylinder), rather than the general time- and space-dependent function $h(\boldsymbol{x}, t)$ predicted by solutions to the governing Equation 1. As we shall see, this assumption of a cylindrical cloud means that velocities inside the cylinder cannot simultaneously satisfy both the mass Equation 1a and momentum Equations 1b and 1c. Under this assumption, conservation of mass Equation 1a, integrated over the extent of the umbrella cloud $0 \le r \le R(t)$, and the boundary condition (Equation 4) express that the volume within the umbrella cloud increases according to the inflow flux,

$$\frac{\mathrm{d}}{\mathrm{d}t}\left(\pi h R^2\right) = Q, \tag{6}$$

where the circular region $r \le R(t)$ is assumed to contain all of the injected material. Rearranging Equations 5 and 6 to eliminate h gives a second order ODE for equation for the cylinder radius $R(t)$,

$$\frac{\mathrm{d}}{\mathrm{d}t}\left(\frac{2\pi}{NFr_f}R^2\frac{\mathrm{d}R}{\mathrm{d}t}\right) = Q. \tag{7}$$

Integrating Equation 7 twice with respect to t, subject to the condition that the cloud is initially empty, $R(0) = 0$, we obtain a $R \sim t^{2/3}$ scaling for the cloud radius,

$$R(t) = \left(\frac{3NFr_fQ}{4\pi}\right)^{1/3} t^{2/3}, \tag{8}$$

as well as expressions for both the thickness of the cylindrical cloud,

$$h(t) = \frac{4}{3}\left(\frac{3Q}{4\pi N^2 Fr_f{}^2}\right)^{1/3} t^{-1/3}. \tag{9}$$

and the spreading rate of the cloud as a function of both time and the current cloud radius,

$$\frac{\mathrm{d}R}{\mathrm{d}t} = \frac{2}{3}Rt^{-1} = \left(\frac{NFr_fQ}{3\pi}\right)^{1/2} R^{-1/2}. \tag{10}$$

Comparison of Equation 8 with the scaling of Woods and Kienle (1994) indicates that the Froude number at the current front Fr_f is related to Woods and Kienle's empirical parameter λ by $\lambda = \mathrm{Fr}_f/2$. There is significant uncertainty in the value of λ but, based on both observation and experiment, it was confined to the interval [0.1, 0.6] by Holasek et al. (1996). The effective value of λ given by the shallow-layer theory of Ungarish (2009) is 0.421. While this is larger than values typically used in the study of ash clouds (Costa et al., 2013; Mastin et al., 2014; Webster et al., 2020), it is within the interval identified by Holasek et al. (1996).

Finally, to develop a parametrization of umbrella cloud spreading, a velocity field inside the cylinder must be chosen; this internal field is not predicted by Woods and Kienle (1994). Webster et al. (2020) extrapolate the front velocity of the cloud (Equation 10) to the entire interior of the cylinder to produce a steady velocity field,

$$u_r^{\mathrm{Webster}} = \left(\frac{NFr_fQ}{3\pi}\right)^{1/2} r^{-1/2}, \tag{11}$$

for $r < R$. Costa et al. (2013) and Mastin et al. (2014) instead derive a velocity field using the assumption of uniform depth and conservation of mass Equation 1a, by substituting the expression (Equation 9) for cylinder depth $h(t)$ into the axisymmetric equivalent of conservation of mass Equation 1a for $0 < r < R$,

$$\frac{\partial h}{\partial t} + \frac{1}{r}\frac{\partial}{\partial r}(hu_r r) = 0, \tag{12}$$

and solving for the radial velocity u_r, subject to the kinematic condition at the front (Equation 4). This gives the radial velocity field used by Costa et al. (2013),

$$u_r^{\mathrm{Costa}} = \frac{3}{4}\frac{\mathrm{d}R}{\mathrm{d}t}\frac{R}{r}\left(1 + \frac{r^2}{3R^2}\right). \tag{13}$$

Whenever used in this paper, the parametrizations (Equations 11 and 13) are employed with $Fr_f = 0.45$ (equivalent to $\lambda = 0.225$), as recommended by Webster et al. (2020).

Although such axisymmetric umbrella cloud parametrizations lead to improved prediction of the extent of an ash cloud, compared to modeling with no umbrella cloud parametrization (Costa et al., 2013; Mastin et al., 2014; Webster et al., 2020), the two major assumptions used in their derivation result in some shortcomings of the resulting parametrizations.

The first assumption, that the dynamics of the umbrella cloud are not affected by wind, exacerbates errors in ash distributions predicted by axisymmetric parametrizations. Because model ash particles are advected by the sum of the meteorological wind and either radial velocity field (Equation 11 or 13), they do not satisfy the kinematic boundary condition (Equation 4) which is formulated under the assumption of a purely radial velocity field. That is, in the presence of any non-zero meteorological wind, model particles exit the downwind edge of the cylinder, and the boundary of the umbrella cloud, as defined by the location of particles, is no longer the cylinder assumed in the derivation of the spreading law. This is problematic because, at the boundary of the cylinder, the wind

field resulting from the sum of meteorological wind and radial umbrella cloud velocity is strongly converging (i.e., the divergence of the three-dimensional velocity field is negative). As highlighted by Webster et al. (2020), this results in a non-physical accumulation of ash at the downwind edge of the cloud. Both polynomial (Webster et al., 2020) and exponential (Folch et al., 2020) smoothing of the umbrella cloud velocity field has been used to mitigate this, by but these smoothings have no physical justification and, as we will demonstrate in Section 3, do not eliminate accumulation. Moreover, model particles that exit the downwind edge of the cloud are no longer subject to buoyancy-driven motion. Consequently, axisymmetric parametrizations cannot reproduce the downwind buoyancy-driven lateral spreading of plumes far downwind of the vent (Bursik, Carey, & Sparks, 1992; Johnson et al., 2015).

The second assumption, that the umbrella cloud is cylindrical and of uniform depth (Equation 9) is central to the derivation of both the $R \sim t^{2/3}$ scaling (Equation 8), and the axisymmetric internal velocity fields suggested by Webster et al. (Equation 11) and Costa et al. (Equation 13). However, crucially, this assumption of a cylindrical cloud is inconsistent with the governing shallow-layer Equation 1, which predict that the cloud depth varies in time and space, even in the absence of wind (Johnson et al., 2015). The effect of this is that the internal velocity fields (Equations 11 and 13) do not satisfy the conservation of momentum. (This can be verified by substituting either velocity field into the axisymmetric form of the momentum Equations 1b and 1c). The shallow-layer model also predicts that, in the absence of wind, the radius of the circular umbrella cloud grows in a more complex manner than the power law $t^{2/3}$. This prediction is consistent with observations of umbrella clouds (Pouget et al., 2016) and occurs because the spatially varying depth of the cloud is not self-similar (Johnson et al., 2015). Consequently, even if the assumption of uniform depth is relaxed in the derivation, there are no internal velocity and thickness fields that simultaneously satisfy mass conservation, momentum conservation and the $R \sim t^{2/3}$ scaling (Equation 8). To derive an internal velocity field for the axisymmetric cloud of Woods and Kienle (1994), an additional choice must therefore be made as to which, if any, of the equations are satisfied. As a consequence, there are many possible velocity fields, of which the velocities of Webster et al. (Equation 11) and Costa et al. (Equation 13) are just two examples. This indeterminacy is problematic, as it is the velocity field which determines the transport and therefore concentration of ash within the cloud.

These shortcomings of axisymmetric parametrizations motivate the presentation of a new non-axisymmetric parametrization in the following section.

2.3. Non-Axisymmetric Simplification of the Shallow-Layer Equations

Instead of assuming an absence of wind and an axisymmetric umbrella cloud, we derive from the shallow-layer mass and momentum partial differential Equation 1. A coupled model for a non-axisymmetric wind-blown umbrella cloud, in which the internal velocities are obtained directly from these physical conservation laws.

The shallow-layer Equation 1, subject to the boundary condition (Equation 3) can be solved numerically (Johnson et al., 2015; Pouget et al., 2016). While this is not practical for rapid operational use in a VATDM, such numerical solutions illustrate two key simplifications that can be made to the governing equations, which lead to a non-axisymmetric umbrella cloud model appropriate for VATDM use.

Numerical solutions of the full system (Equations 1 and 3) show that, for axisymmetric currents spreading in a stationary atmosphere, a balance between buoyancy and turbulent drag is rapidly established within the cloud (Johnson et al., 2015). The same spreading dynamics occur for clouds in a uniform wind, where numerical solutions and asymptotic analysis of Equations 1 and 3 indicate spreading far downstream is again dominated by a balance between buoyancy and turbulent drag (Johnson et al., 2015). This transition to a turbulent-drag/buoyancy balance is supported by measurements of volcanic umbrella clouds from satellite imagery (Pouget et al., 2016). The first simplification made is therefore to reduce the momentum Equations 1b and 1c by neglecting inertial terms, reflecting the established balance of forces. In addition, the boundary condition at the flow front (Equation 3) is neglected in favor of enforcing zero depth, $h = 0$, due to the relative unimportance of energy losses at the flow front on spreading dynamics in the drag/buoyancy regime.

For umbrella clouds resulting from a sustained constant volume flux, numerical solutions and asymptotic solutions of the full system (Equations 1 and 3) also quickly adopt near-steady state thickness and velocity fields within the cloud, in both uniform wind (Johnson et al., 2015, Equation 4.7) and in a static atmosphere (Baines, 2013; Johnson et al., 2015, Equation 3.30), with modest discrepancies from this steady state only close to the advancing

cloud front. The second simplification is therefore to approximate the velocity field within the cloud as steady, by dropping time derivatives from Equation 1.

Finally, we exploit the fact that drag-dominated solutions of Equation 1 depend primarily on the inflow volume flux and not other properties of the source (Johnson et al., 2015), to write the source function q as a point source with a Dirac delta function,

$$q(\boldsymbol{x}) = Q\delta(\boldsymbol{x}). \tag{14}$$

Under the approximations above, the mass and momentum Equation 1 reduce to

$$\nabla \cdot (h\boldsymbol{u}) = Q\,\delta(\boldsymbol{x}), \tag{15a}$$

$$N^2\frac{h^2}{4}\nabla h = -C_D(\boldsymbol{u}-\boldsymbol{U})|\boldsymbol{u}-\boldsymbol{U}|. \tag{15b}$$

Remarkably, all parameters of the new governing Equation 15 can be scaled out by non-dimensionalizing using the length and time scales

$$L_H = \left(\frac{Q^3N^2}{C_DU^5}\right)^{1/4}, \quad L_V = \left(\frac{C_DQU}{N^2}\right)^{1/4}, \quad T = L_H/U = \left(\frac{Q^3N^2}{C_DU^9}\right)^{1/4}, \tag{16}$$

where L_H and L_V are distinct horizontal and vertical lengthscales. In non-dimensional (starred) variables,

$$x^\star = \frac{x}{L_H}, \quad y^\star = \frac{y}{L_H}, \quad h^\star = \frac{h}{L_V}, \quad \boldsymbol{u}^\star = \frac{\boldsymbol{u}}{L_H/T}, \tag{17}$$

Equation 15 is a parameterless system of PDEs for the non-dimensional quantities $\boldsymbol{u}^\star$ and $h^\star$,

$$\nabla^\star \cdot \left(h^\star\boldsymbol{u}^\star\right) = \delta^\star\left(\boldsymbol{x}^\star\right), \tag{18a}$$

$$\frac{h^{\star 2}}{4}\nabla^\star h^\star = -\left(\boldsymbol{u}^\star - \boldsymbol{e}_x\right)\left|\boldsymbol{u}^\star - \boldsymbol{e}_x\right|, \tag{18b}$$

where $\boldsymbol{e}_x$ is the unit vector in the x-coordinate direction.

The parameterless nature of the system (Equation 18) is crucial to its suitability for operational use, as the solution to Equation 18 can be precalculated once and stored. To obtain the solution to Equation 15 in the VATDM, for a cloud generated by any eruption, the precalculated solution to Equation 18 is simply scaled by the appropriate length and time scales (Equation 16), obtained using Q, N, U, and C_D for the eruption in question.

To numerically solve the simplified governing Equation 18, we rearranged Equation 18b to obtain

$$\boldsymbol{u}^\star = \boldsymbol{e}_x - \frac{h^\star\nabla^\star h^\star}{2\sqrt{|\nabla^\star h^\star|}}. \tag{19}$$

and substituted this into (Equation 18a), giving an equation for $h^\star$,

$$\nabla^\star \cdot \left(h^\star\boldsymbol{e}_x - \frac{h^{\star 2}\nabla^\star h^\star}{2\sqrt{|\nabla^\star h^\star|}}\right) = \delta^\star\left(\boldsymbol{x}^\star\right). \tag{20}$$

We solved this equation by time-integrating to steady state the equivalent parabolic problem (Equation 20) with an additional $\partial h^\star/\partial t^\star$ term on the left hand side), using the finite volume method of Kurganov and Tadmor (2000). The resulting non-axisymmetric solution for the depth is illustrated in Figure 1. From this solution for $h^\star$, the velocity field within the umbrella cloud $\boldsymbol{u}^\star$ can be recovered using Equation 19. Streamlines of this velocity field are illustrated in Figure 1.

The velocity field (Equation 19) is the solution to a system of physically meaningful conservation laws, with mass and momentum equations solved simultaneously. These conservation laws are consistent with an umbrella cloud spreading in a uniform wind, where the dynamics of the cloud are governed by a balance between turbulent drag

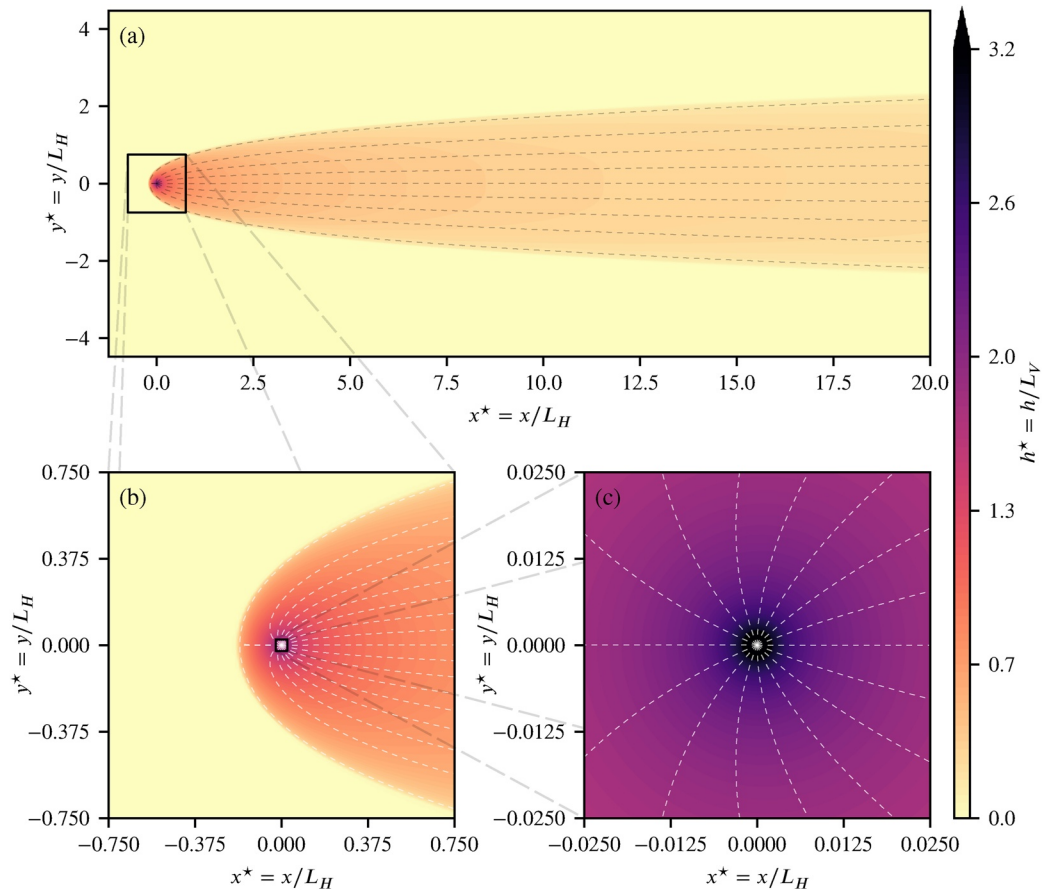

Figure 1. Solution of the non-dimensional wind-blown umbrella cloud model (Equation 18), showing the depth of a wind-blown umbrella cloud (shading) and streamlines of the velocity field (Equation 19), which correspond to particle trajectories (dashed lines). All three panels show the same solution at different scales. Panel (a) shows the downwind motion and buoyancy-driven lateral spreading far from the source, and the approach to the far-downwind asymptotic solution discussed in Appendix A. Zooming in, panel (b) shows the upwind stagnation point and redirection of near-axisymmetric flow near the source to predominantly downwind motion. Panel (c) shows the near-axisymmetric structure of the solution near the source.

from a moving atmosphere and buoyancy forces. Although the system (Equation 18) is simplified compared to the full shallow-layer equations, these simplifications are justified by the close similarity between solutions to the simplified system and solutions of the full shallow-layer equations. In fact, the simplified system (Equation 18) has identical solutions to the full shallow-layer system (Equations 1 and 3) in the asymptotic limits of flow both close to the source and far downwind, as shown in the Appendices (Appendix A1 and A2, respectively).

2.4. Non-Axisymmetric Parametrization of a Wind-Blown Umbrella Cloud

Having constructed a non-axisymmetric simplification of a wind-blown umbrella cloud, we now outline how it can be used to modify Lagrangian trajectories in a VATDM, using a three-dimensional wind field from a numerical weather prediction (NWP) model. We use the NAME software as an example.

Given a model Lagrangian particle in NAME, with position $\boldsymbol{x}_i(t)$ at time t, the position of this particle at time $t + \Delta t$ is given by

$$\boldsymbol{x}_i(t + \Delta t) = \boldsymbol{x}_i(t) + \boldsymbol{u}_M(\boldsymbol{x}_i(t), t)\Delta t + \boldsymbol{D}_w(\boldsymbol{x}_i(t), t) + p(\boldsymbol{x}_i(t), t). \quad (21)$$

The first two terms on the right hand side represent a first-order Euler approximation of the advection of the particle by the NWP wind field $\boldsymbol{u}_M$. The next term $\boldsymbol{D}_w(\boldsymbol{x}_i(t), t)$ represents the displacement of the particle during this time step by the umbrella cloud, and is the quantity to be calculated here. The final term p represents all

other physical processes implemented in NAME that influence the particle position, but here are assumed to be independent of the umbrella cloud, for example, particle sedimentation and turbulent diffusion.

The umbrella cloud increment $\boldsymbol{D}_w(\boldsymbol{x}_i(t),\ t)$ is calculated by integrating a particle trajectory through the non-dimensional umbrella cloud wind field $\boldsymbol{u}^\star(x^\star,\ y^\star)$ (Figure 1), then redimensionalizing this trajectory using the scalings (Equation 16) so that it corresponds to the desired eruption and wind conditions.

A particle at position $\boldsymbol{x}^\star(t^\star)$ advected by the non-dimensional velocity field moves according to the equation

$$\frac{\mathrm{d}\boldsymbol{x}^\star}{\mathrm{d}t^\star} = \boldsymbol{u}^\star\left(\boldsymbol{x}^\star\right). \tag{22}$$

This equation can be solved analytically for particles very near the source $|\boldsymbol{x}^\star| \ll 1$ or far downstream $x^\star \gg 1$ (Appendix A). Elsewhere, a solution can be obtained by integrating the ordinary differential Equation 22 numerically (e.g., using a Runge-Kutta method), with the wind field inside the umbrella cloud $\boldsymbol{u}^\star$ evaluated using numerical interpolation of the pre-calculated solution to Equation 19. Whether solutions to Equation 22 are obtained analytically or numerically, they allow evaluation of the displacement $\boldsymbol{d}_w^\star\left(\boldsymbol{x}_0^\star, \Delta t^\star\right)$ that occurs when a Lagrangian particle with trajectory $\boldsymbol{x}^\star(t^\star)$ starts at position $\boldsymbol{x}^\star(0) = \boldsymbol{x}_0^\star$ and is advected for a time $\Delta t^\star$. That is,

$$\boldsymbol{d}_w^\star\left(\boldsymbol{x}_0^\star, \Delta t^\star\right) = \boldsymbol{x}^\star\left(\Delta t^\star\right) - \boldsymbol{x}_0^\star, \tag{23}$$

where $\boldsymbol{x}^\star(t^\star)$ is a solution to the equation of motion (Equation 22). When $\boldsymbol{d}_w^\star$ is calculated numerically, an appropriate time step is chosen to ensure an accurate solution regardless of the size of the time increment $\Delta t^\star$ over which the displacement $\boldsymbol{d}_w^\star$ is evaluated. Note that since the non-dimensional wind field $\boldsymbol{u}^\star$ includes both the background wind (assumed uniform over the interval $\Delta t^\star$) and the wind due to the umbrella cloud, the displacement $\boldsymbol{d}_w^\star$ is the displacement due to both umbrella cloud and wind.

The dimensional displacement $\boldsymbol{D}_w(\boldsymbol{x}_i(t),\ t)$ in Equation 21 represents the displacement due to the umbrella cloud alone; it is evaluated by first subtracting the background wind from the non-dimensional displacement $\boldsymbol{d}_w^\star$ to obtain the non-dimensional displacement due to the umbrella cloud alone, then scaling and rotating this, according the meteorological wind field and eruption parameters. For a given eruption, the parameters Q, N, and C_D are chosen (using the protocol given in Section 3.1) and fixed for the duration of the eruption. To determine U we sample the velocity of the NWP wind field at the current time and particle location, $\boldsymbol{u}_M(\boldsymbol{x}_i(t),\ t) = (u_M,\ v_M,\ w_M)$ and evaluate its horizontal speed,

$$U = \sqrt{u_M^2 + v_M^2}. \tag{24}$$

These parameters are used to compute length and timescales using Equation 16. The angle between the NAME coordinate x-axis and wind velocity

$$\psi = \arctan\left(\frac{u_M(\boldsymbol{x}_i(t), t)}{v_M(\boldsymbol{x}_i(t), t)}\right), \tag{25}$$

is then used to construct the rotation matrices

$$\mathbf{M} = \begin{pmatrix} \cos\psi & \sin\psi \\ -\sin\psi & \cos\psi \end{pmatrix}, \quad \mathbf{M}^{-1} = \begin{pmatrix} \cos\psi & -\sin\psi \\ \sin\psi & \cos\psi \end{pmatrix}, \tag{26}$$

that define a transformation and its inverse from NAME Cartesian coordinates to coordinates with basis vectors tangent and normal to the local in-plane wind direction. (Without loss of generality, we take the origin of the dimensional coordinate $\boldsymbol{x}$, like that of the non-dimensional $\boldsymbol{x}^\star$, to be at the volcano vent, so that this rotation occurs around the position of the vent.) The resulting increment in particle position due the umbrella cloud for a particle currently at position $\boldsymbol{x}$ is then,

$$\boldsymbol{D}_w(\boldsymbol{x}, t) = L_H \mathbf{M}^{-1}\left[\boldsymbol{d}_w^\star\left(\frac{1}{L_H}\mathbf{M}\boldsymbol{x},\ \frac{1}{T}\Delta t\right) - \frac{1}{T}\Delta t \boldsymbol{e}_x\right]. \tag{27}$$

This increment defines the wind-blown umbrella cloud parametrization proposed in this paper.

Substituting the increment Equation 27 into Equation 21, and simplifying, gives

$$\boldsymbol{x}_i(t+\Delta t) = \boldsymbol{x}_i(t) + \begin{pmatrix} 0 \\ 0 \\ w_M(\boldsymbol{x}_i(t),t) \end{pmatrix} \Delta t + L_H \mathbf{M}^{-1} \boldsymbol{d}_w^{\star}\left(\frac{1}{L_H}\mathbf{M}\boldsymbol{x}, \frac{1}{T}\Delta t\right) + p(\boldsymbol{x}_i(t),t). \tag{28}$$

Comparing to Equation 21, we see that the scheme is equivalent to applying first-order Euler integration of meteorological wind to the vertical component w_M only. The advection of a particle by the horizontal components of the wind, now perturbed by the umbrella cloud, is calculated by integration of the trajectory Equation 22 to obtain $\boldsymbol{d}_w^{\star}$, with appropriate scaling by L_H and rotation to by angle ψ. The other physical processes influencing the particle position, parametrized by the function p, are unchanged. This scheme is self-consistent in a steady uniform meteorological wind, in the sense that particle trajectories calculated by the VATDM are then exactly the trajectories of the solution to the partial differential Equation 15.

The dependence of the model on the three parameters C_D, Q, and N is simplified by the fact that these occur in Equation 27 solely through the scales L_H and T, which can be written as $L_H = \sqrt[4]{K/U^5}$, $T = \sqrt[4]{K/U^9}$, where

$$K = Q^3 N^2 / C_D. \tag{29}$$

Since the dependence of the parametrization on N, Q, and C_D is only through the group K, all combinations of these parameters that have the same value of K produce identical model results.

The scaling L_H applied to the non-dimensional displacement $\boldsymbol{d}_w^{\star}$, illustrates how the magnitude of wind and volume flux influence the predicted umbrella cloud. In the case of a small volume flux (small Q) and/or rapid wind (large U), the lengthscale L_H becomes small. The scale of the non-dimensional umbrella cloud is therefore small, and the buoyancy-driven perturbation to the wind field experienced by model particles will then be highly non-axisymmetric, as shown in Figure 1a, with buoyancy driving lateral spreading of a wind-blown plume. In the limit of very small flux ($Q \to 0$), L_H also vanishes and the meteorological wind field is unmodified, recovering the VATDM behavior without an umbrella cloud parametrization. Conversely, for a large volume flux and/or light wind the lengthscale L_H becomes large. The scale of the non-dimensional umbrella cloud is therefore also very large, and as illustrated in Figure 1c, Lagrangian particles experience a near-axisymmetric perturbation of the meteorological wind field, as expected for a circular umbrella cloud formed in light winds.

The power-law dependence of L_H on Q, N, C_D, and U (Equation 16) allows the sensitivity of the umbrella cloud scheme to these parameters to be determined straightforwardly. In a uniform wind, the upwind spreading distance of the umbrella cloud scales as L_H, while, for strongly wind-blown plumes, the width of the plume at a fixed location scales as $L_H^{2/3}$, due to the width of the plume scaling as the cube root of the downwind distance (Equation A22). Since $L_H \sim Q^{3/4} N^{1/2} C_D^{-1/4} U^{-5/4}$, each percent increase in volume flux Q leads to 0.75% increase in upstream spread and a 0.5% increase in lateral spread, each percent increase in C_D leads to 0.25% decrease in upstream spread and a 0.17% decrease in lateral spread, while each percent increase in the meteorological wind U leads to 1.25% decrease in upstream spread and a 0.87% decrease in lateral spread.

3. Validation

To test the validity of the assumptions in the new non-axisymmetric umbrella cloud model, we apply it to four eruptions (Puyehue-Cordón Caulle 2011, Pinatubo 1991, Ulawun 2019, and Calbuco 2015) and compare the resulting ash column loadings with satellite observations of the cloud boundary and predictions of the existing axisymmetric parametrization of Webster et al. (2020). These eruptions span a wide range of volume fluxes and wind speeds, resulting in umbrella clouds ranging from near-axisymmetric to strongly wind-blown. For consistency with previous studies (e.g., Costa et al., 2013; Van Eaton et al., 2016; Webster et al., 2020), satellite brightness temperature contours are used to indicate umbrella cloud extent, with identical contours to Webster et al. (2020) used where possible to enable direct comparison.

3.1. Determining Model Parameters

We first discuss how the three parameters of the non-axisymmetric parameterization, C_D, N, and Q, are chosen.

The coefficient of turbulent skin drag C_D is not well constrained for volcanic ash clouds. Based on laboratory experiments by Abraham et al. (1979), Baines (2013) suggested that $C_D = 8 \times 10^{-4}$ is an appropriate choice for umbrella clouds. Johnson et al. (2015) suggested that when applied to a system of shallow-layer equations such as Equation 1, a suitable order of magnitude estimate is $C_D = 0.01$. Numerical solutions of the shallow-layer Equation 1 have been compared to satellite observations of umbrella clouds in two studies: Pouget et al. (2016), who assumed a stationary atmosphere, and de' Michieli Vitturi and Pardini (2021), who assumed a steady and spatially uniform wind field. Both studies found $C_D = 0.1$ to be suitable. To reflect the wide range of values in the literature, for each case study we use $C_D = 0.001$, 0.01 and 0.1.

The buoyancy frequency N is a measure of the stratification of the stable atmosphere at the altitude of the umbrella cloud, and is generally available as an output of NWP models. Full 3-D numerical simulations of volcanic plumes by Suzuki and Koyaguchi (2009) found $N \sim 0.02$ s^{-1} for both midlatitude and tropical conditions. Webster et al. (2020) state $N = 0.02$ s^{-1} is generally suitable for stratospheric eruptions. We therefore take $N = 0.02$ s^{-1} for each eruption considered.

The volume flux at neutral buoyancy level Q is often one of the major uncertainties in volcanic plume models, and many methodologies for estimating this have been proposed. To enable direct comparison of results, we use the same methodologies as Webster et al. (2020), which are summarized here. In Morton et al. (1956)'s influential study of buoyant plumes in a stratified atmosphere, a relationship between the maximum rise height of the plume above vent level (avl) H_T and the vertical volume flux at the neutral buoyancy level is determined. If it is assumed that this vertical flux is equal to the flux into the umbrella cloud, then

$$Q = C_v N {H_T}^3, \tag{30}$$

where C_v is a constant to be determined. Several researchers have derived or measured values for the constant C_v. Using the more complex plume model of Bloomfield and Kerr (2000), Rooney and Devenish (2014) computed numerical solutions which indicated $C_v = 0.0111$ (referred to as model BK). Large eddy simulations of the Boussinesq equations computed by Devenish et al. (2010) imply $C_v = 0.00939$ (model D). Finally, 3D Navier-Stokes simulations of plumes, carried out by Suzuki and Koyaguchi (2009) confined C_v to the range [0.0160, 0.0382] for tropical conditions and [0.0103, 0.0221] for mid-latitude conditions. For each eruption, we use a value of C_v corresponding to the closest match between observation and the values of H_T considered by Suzuki and Koyaguchi (2009) (model SK). An alternative approach (model B) is offered by Bursik, Sparks, et al. (1992), who obtained the power law fit

$$H_T = 287 Q^{0.19} \tag{31}$$

of the numerical results of Sparks (1986) and Woods (1988), which in turn are obtained from modified versions of the original Morton et al. (1956) model. In Equation 31, H_T and Q are dimensional quantities with units m and m^3 s^{-1}, respectively.

The solids mass eruption rate into the neutral buoyancy level M_N, in kg s^{-1}, is necessary to generate predictions of ash column loading, but does not influence the umbrella cloud parametrization. This is computed from the plume rise height using the empirical formula of Mastin (2014),

$$M_N = 140\left(\frac{H_T + H_V}{1000}\right)^{4.15}, \tag{32}$$

where H_V is the volcano vent height measured in meters above sea level. Following the procedure used at the London VAAC for operational modeling (Witham et al., 2019), it is assumed that the distal fine ash fraction (the fraction of the mass flux into the cloud predicted by Mastin (2014) that is not deposited close to the source) is 5%, and an ash mass flux $M_T = 0.05 M_N$ is therefore used. We use the standard particle size distribution used by the London VAAC for all eruptions (Webster et al., 2012).

The umbrella cloud height H_U is usually smaller than the maximum rise height H_T and is inferred from satellite observations for all eruptions studied in this paper. However, in practice, H_U can be hard to determine and is sometimes unavailable, at least in time for operational use. In this case, Webster et al. (2020) recommend the upper surface of the umbrella cloud H_U (avl) should be set as $0.8 H_T$. The cloud depth $0.15 H_T$ is used, such that ash is released over the height interval $[H_U, H_U - 0.15 H_T]$, relative to the elevation of the vent.

Table 1
Eruption Parameters, Inferred Volume Fluxes From Each Model, and Numerical Weather Prediction (NWP) Model Information Used for Each Case Study

	Puyehue	Pinatubo	Ulawun	Calbuco
Start date	2011-06-04[a]	1991-06-15[e]	2019-06-26[h]	2015-04-23[k]
Start time (UTC)	18:45[a]	04:40[e]	06:00[h]	04:00[k]
End date	2011-06-05[b]	1991-06-15[e]	2019-06-26[h]	2015-04-23[k]
End time (UTC)	22:00[b]	13:40[e]	07:10[h]	10:00[k]
Summit elevation (m)	2236[c]	1745[f]	2334[i]	1974[l]
H_T (km avl)	10[c]	37[e]	23.8[h]	21[m]
H_U (km avl)	11.2[d]	25[e]	16.7[j]	17[k]
Q (m^3s^{-1}) (D)	1.86×10^8	9.51×10^9	2.53×10^9	1.74×10^9
Q (m^3s^{-1}) (BK)	2.20×10^8	1.12×10^{10}	3.00×10^9	2.06×10^9
Q (m^3s^{-1}) (SK)	6.00×10^8	3.86×10^{10}	3.87×10^9	2.66×10^9
Q (m^3s^{-1}) (B)	1.28×10^8	1.28×10^{11}	1.25×10^{10}	6.50×10^9
Q (m^3s^{-1}) (P)	-	5.8×10^{10}[g]	-	-
Q (m^3s^{-1}) (VE1)	-	-	-	5.93×10^{10}[k]
Q (m^3s^{-1}) (VE2)	-	-	-	7.80×10^{10}[k]
M_T (kg s^{-1})	2.26×10^5	2.26×10^7	5.13×10^6	3.04×10^6
Volcanic explosivity index (VEI)	5[a]	6[f]	4[i]	4[l]
NWP	Global MetUM (Met Office) $0.3516° \times 0.2344°$	ERA-Interim (ECMWF) $0.75° \times 0.75°$	Global MetUM (Met Office) $0.141° \times 0.094°$	Global MetUM (Met Office) $0.234° \times 0.156°$

[a]Collini et al. (2013). [b]Jay et al. (2014). [c]Global Volcanism Program (2012). [d]Prata et al. (2021). [e]Holasek et al. (1996). [f]Global Volcanism Program (1991). [g]Mastin et al. (2014). [h]McKee et al. (2021). [i]Global Volcanism Program (2019). [j]Horváth et al. (2021). [k]Van Eaton et al. (2016). [l]Global Volcanism Program (2015). [m]Vidal et al. (2017).

For each case study, the overshooting plume top heights, umbrella cloud heights, derived mass and volume fluxes, and meteorological data sets, together with their sources, are given in Table 1.

Meteorological wind fields from the Met Office Global Unified Model are used for all case studies except Pinatubo 1991, for which historical data from the Met Office are not archived; the ECMWF ERA-Interim reanalysis data set is used instead, as in Costa et al. (2013), Mastin et al. (2014), and Webster et al. (2020).

3.2. Puyehue, 2011

The climactic phase of the 2011 Puyehue-Cordón Caulle eruption began at 18:45 UTC on the fourth of June and continued for approximately 27 hr, producing a ribbon-like ash cloud that spread as far east as the Atlantic Ocean (Collini et al., 2013). Aerial photographs of the eruption column (Collini et al., 2013) show a strong plume with clear upwind spreading characteristic of an umbrella cloud, which extended ∼10 km upwind of the vent. The spread of the cloud at 15:25 UTC on 5 June 2011 was captured by a MODIS instrument aboard NASA's Terra satellite.

NAME runs using the new wind-blown parametrization were computed for each combination of drag coefficient given in Section 3.1 and volume flux detailed in Table 1. Additionally, Webster et al. (2020)'s parametrization of umbrella cloud spreading is used for each volume flux. The same set of runs are computed for each of the subsequent case studies in Sections 3.3–3.5, with parameters from the appropriate column in Table 1.

Figure 2 shows with yellow-purple shading ash column loadings predicted by NAME model runs (a) without an umbrella cloud parametrization, (b–d) with Webster et al. (2020)'s parametrization for the smallest, an

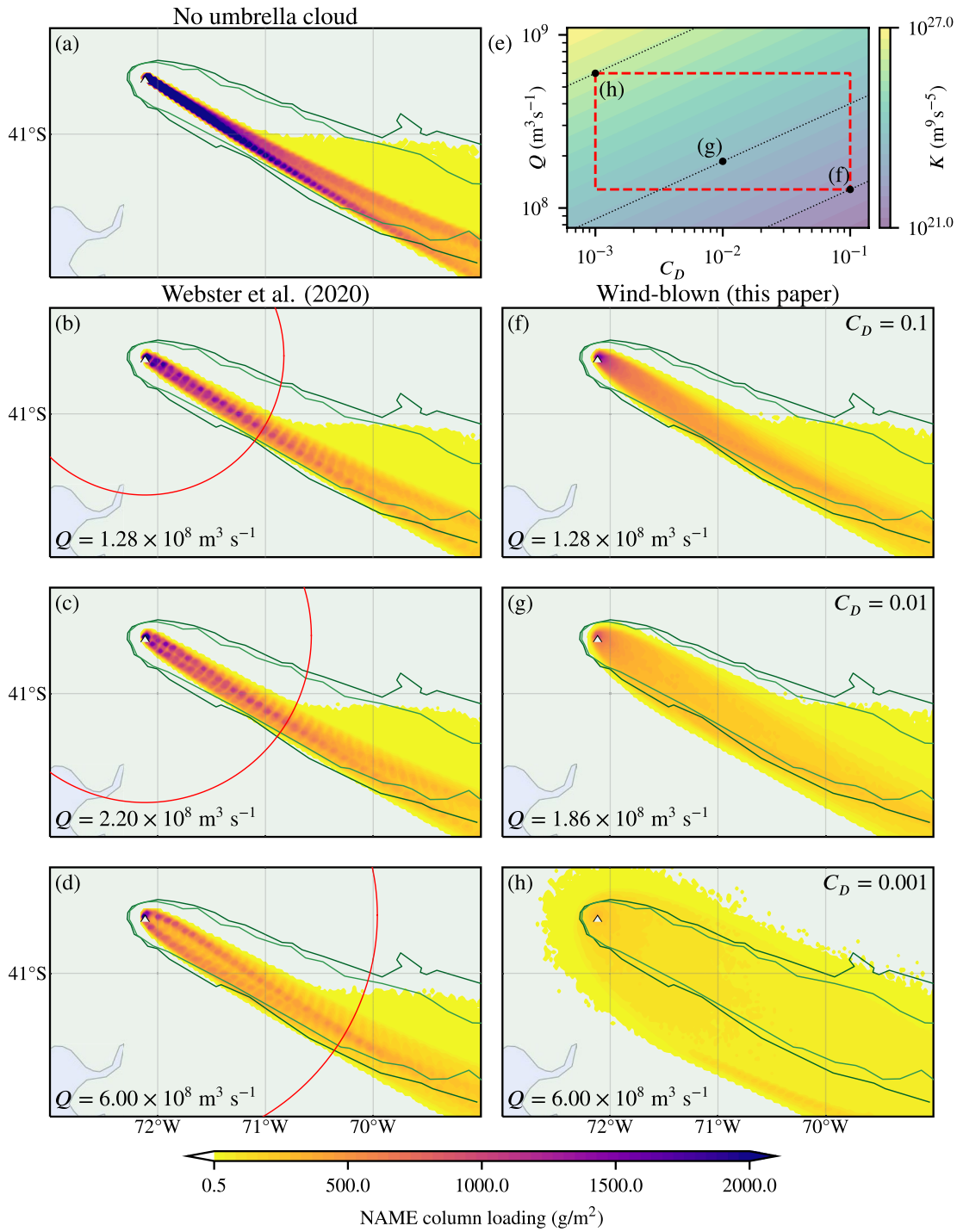

Figure 2. Numerical Atmospheric-dispersion Modeling Environment (NAME) simulations of the climactic phase of the 2011 Puyehue eruption at 15:25 UTC. Ash column loadings are illustrated by the yellow/purple heatmap, overlaid with green contours of 11 μm brightness temperature at 225 and 235 K (light to dark). Panel (a) does not use an umbrella parametrization. Panels (b–d) use the axisymmetric parametrization (Equation 11) with volume fluxes predicted by models (B), (BK), and (SK), respectively. Panel (e) maps the parameter space of the wind-blown parametrization. Red circles in panels (b–d) illustrate the boundary of the umbrella region (Equation 8). Panels (f–h) use the wind-blown parametrization with volume fluxes predicted by models (B), (D), and (SK), respectively.

intermediate, the largest volume flux in Table 1, and (f–h) the wind-blown plume parametrization for the smallest, best-fit and largest values of $K = Q^3N^2/C_D$. An intermediate flux is used for panel (c) because the best fit to observations of the Webster et al. (2020) model is here obtained at the largest volume flux, shown in panel (d).

Green contours show satellite observations of the extent of the plume, here contours of 225 and 235 K brightness temperature obtained from the 13 μm MODIS band. The red circle in panels (b–d) show the size and shape of the axisymmetric umbrella cloud in the parametrization of Webster et al. (2020), given by Equation 8, within which particles are influenced by the umbrella cloud. Figure 2e shows diagrammatically how each value of K used in panels (f–h) corresponds to a range of parameters C_D and Q that produce the same model results.

Figure 2 (and all subsequent Figures 3–5) shows ash concentrations at the time of eruption cessation. A time series of images showing the evolution of ash concentration throughout the period of eruption for each case study is provided in the Supporting Information (Figures S1–S12 in Supporting Information S1). For each case study in Figures 2–5, the results in the center panels (c) (Webster et al., 2020, parametrization) and (g) (wind-blown parametrization of this paper) show results for the values of Q and K, respectively, that best match observations—unless the best match occurs at the largest or smallest value of these parameters, in which case an intermediate parameter value is shown.

Predictions of ash column loading below 0.5 g m^{-2} are not plotted. This loading is a conservative estimate for the minimum ash column loading detectable by satellite instruments (Webster et al., 2020). Therefore, the boundary of the yellow shading is representative of the predicted boundary the umbrella cloud and is comparable to the satellite observations.

Both the modeling without an umbrella cloud and the axisymmetric parametrization of Webster et al. (2020) (panels a–d) significantly underpredict the upwind and crosswind spreading of the plume, for all values of the volume flux. Because the ash only occupies a small sector of the modeled circular umbrella cloud in the axisymmetric parametrization, the dominant effect of this parametrization is to increase the speed at which ash is advected downwind, without significant lateral spreading; this is reflected in the under-prediction of lateral spreading in results.

Conversely, in the wind-blown parametrization (panels f–h), crosswind spreading is modeled along the entire length of the cloud, along with upwind spreading close to the source, due to the incorporation of wind in the umbrella cloud dynamics. The wind-blown parametrization predicts a greater upwind and crosswind spreading, with a plume shape that is in good agreement with the observations for the median parameter values in panel (g).

In the axisymmetric parametrization, the predicted column loading at the largest flux Q (panel d) is greater at the edges of the plume than in the center (a phenomenon that can be seen too in the Calbuco case study, Figures 5b–5d). This surprising prediction is a numerical artifact of the size of the NAME time step, which is set by the NWP wind speed and grid cell size, not the velocity field obtained when the NWP wind field is summed with the radial perturbation (Equation 11). The time step taken by NAME can become too large to accurately resolve trajectories of the combined velocity field, leading to errors like those seen in Figure 2d. Such artifacts are avoided in the wind-blown parametrization by use of sub-time stepping of the umbrella cloud trajectories, using smaller time steps than the main NAME time step.

The improved performance of the wind-blown parametrization over axisymmetric parametrizations is unsurprising for strongly wind-affected eruptions like that at Puyehue, since the inclusion of wind in the umbrella cloud dynamics is clearly justified for such eruptions. However, as a tool intended for operational use it is crucial that the wind-blown parametrization can accurately model eruptions in a wide range of wind conditions, including relatively still atmospheres. Accordingly, we now test the parametrization in two progressively more axisymmetric and less wind-affected eruptions, at Pinatubo and Ulawun.

3.3. Pinatubo, 1991

Following weeks of increasing seismic and eruptive activity, on 15 June 1991 Mount Pinatubo underwent a climactic eruption which generated a large stratospheric umbrella cloud covering an area of over 230,000 km^2 (Holasek et al., 1996). The umbrella cloud developed over a 9 hr period in which it was continuously supplied by the volcanic plume, the largest sustained eruption in the satellite era (Lynch & Stephens, 1996). Owing to the prevailing wind direction, the ash cloud spread predominantly in a south westerly direction, but nonetheless having ∼250 km of upwind spread to the north east.

The spread of the umbrella cloud was captured by instruments aboard the geostationary satellite Himawari-4. Analysis of thermal IR data by Holasek et al. (1996) produced a set of contours describing the evolution of the

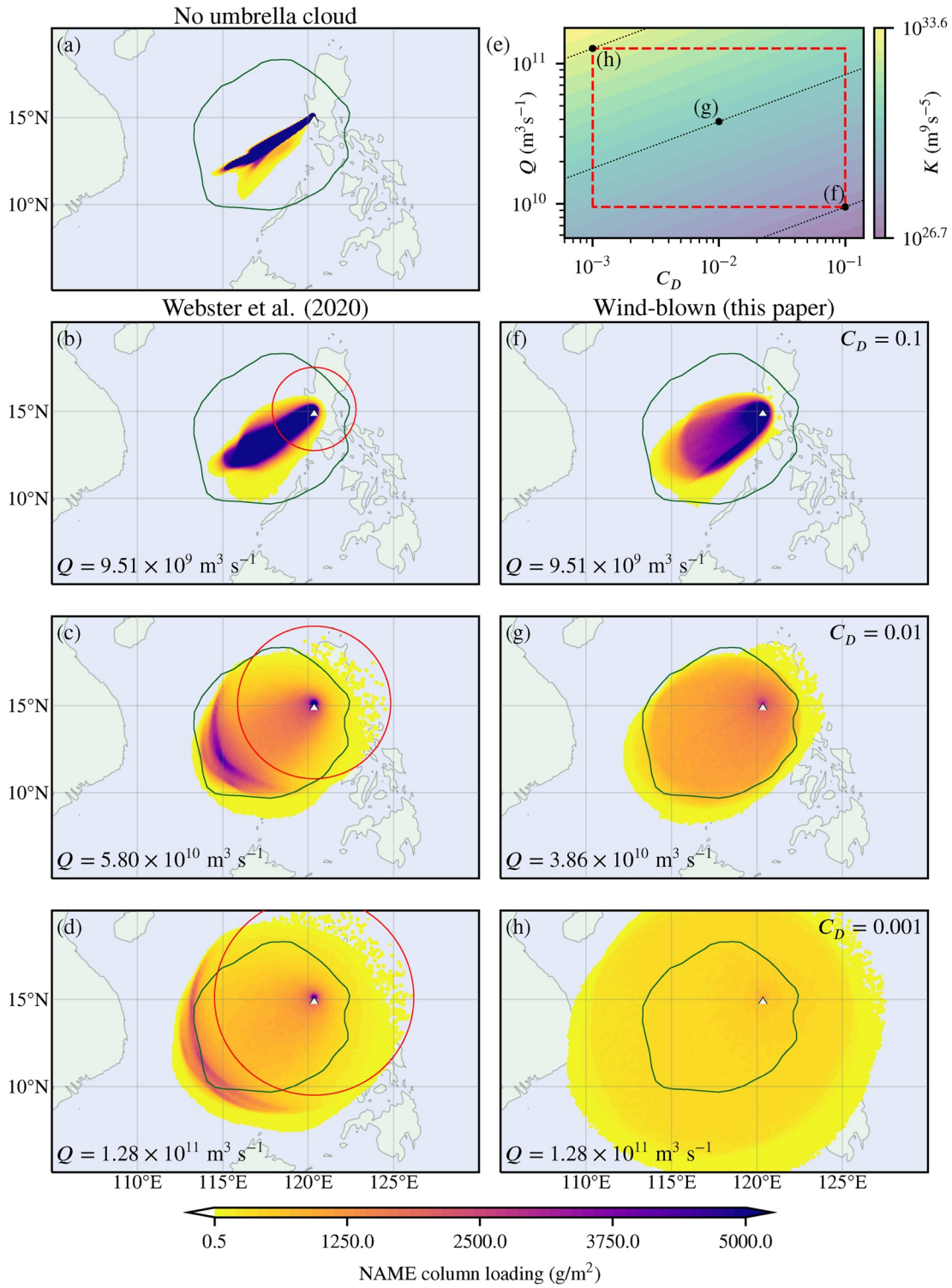

Figure 3. Numerical Atmospheric-dispersion Modeling Environment (NAME) simulations of the 1991 Pinatubo eruption at 13:41 UTC. Ash column loadings are illustrated by the yellow/purple heatmap, overlaid with green contours of the visible cloud edge. Panel (a) does not use an umbrella parametrization. Panels (b–d) use the axisymmetric parametrization (Equation 11) with volume fluxes predicted by models (D), (P), and (B), respectively. Red circles in panels (b–d) illustrate the boundary of the umbrella region (Equation 8). Panel (e) maps the parameter space of the wind-blown parametrization. Panels (f–h) use the wind-blown parametrization with volumes fluxes predicted by models (D), (SK), and (B), respectively.

detectable edge of the cloud during the interval 04:40–15:40 UTC which are used by Costa et al. (2013) and Webster et al. (2020), and in this study.

Costa et al. (2013) noted that, compared to the evolution of the Pinatubo umbrella cloud, the ERA-Interim wind fields do not match the prevailing direction or speed of the umbrella cloud's spread. This discrepancy is partially attributed to the contemporary presence of a typhoon in the region. Costa et al. (2013) suggest that the wind field be rotated by 30° about the volcano vent, and halved in magnitude, whereas subsequent studies (Mastin et al., 2014; Webster et al., 2020) have rotated the wind field but not altered its magnitude. To ensure that any differences in the comparison between our results and those of Webster et al. (2020) are due to the new parametrization only, we follow Webster et al. (2020) in modifying wind direction but not magnitude.

The predicted ash column loadings are shown in Figure 3, with panels having the same meaning as in Figure 2. Panel (a) illustrates a run with no umbrella cloud parametrization. For Webster et al. (2020)'s parametrization, Figure 3 shows runs for (b) the smallest and (d) largest volume fluxes, as well as (c) the optimal volume flux of those investigated by Webster et al. (2020), that given by of Mastin et al. (2014), model (P).

For the wind-blown parametrization, Figure 3 illustrates runs for (f) the smallest, (g) best, and (h) largest values of parameter K considered, illustrated by the dashed rectangle in the map of the parameter space in panel (e).

Because of the uncertainty, the wide range of volume flux predictions offered by the plume models considered, and the uncertainty in the value of C_D, both the wind-blown and Webster et al. (2020)'s axisymmetric parametrization can both underestimate and overestimate the cloud spread, depending on the parameters chosen. This is partly due to the large uncertainty in Q for this case study. For mid-range values, generally good agreement with the observed boundary of the cloud is obtained with both parametrizations.

However, all simulations using the axisymmetric parametrization exhibit a substantial increase in predicted column loading near the downwind leading edge of the cloud. This is due to modeled particles leaving the cylindrical umbrella cloud region (red circle in Figures 3b–3d) and encountering the converging velocity field at the boundary between the umbrella-cloud region and the undisturbed meteorological wind surrounding it. Such accumulation effects are significantly reduced in the wind-blown scheme because the umbrella cloud velocity field (Equation 19) is both coupled with the meteorological wind and has no downwind boundary through which particles can exit.

The range of cloud sizes predicted across the full range of parameter values is greater for the wind-blown parametrization. This is, in part, because the only parameter we vary in Webster et al. (2020)'s model is the flux Q (with other parameters set to recommended values), whereas both C_D and Q are varied in the wind-blown parametrization, with runs selected to cover the widest possible range of the parameter $K = Q^3N^2/C_D$. The cubic dependence of K on Q but reciprocal dependence on C_D, means that the wind-blown parametrization is intrinsically more sensitive to variations in Q than to variations in C_D. Variation of C_D across the full range 0.001–0.1 considered (a factor of 100) therefore accounts for a smaller variation in K than the factor of ∼13 difference between the largest and smallest model estimates of Q in Table 1 (Figure 3e). The broad range of predicted cloud sizes is therefore due to variation of both C_D and Q, but primarily the latter in this case.

3.4. Ulawun, 2019

In the summer of 2019, the Ulawun volcano in New Britain, Papua New Guinea erupted twice, first on the 26 June and then again on the 3 August. The 26 June eruption began with a sub-Plinian degassing phase, followed by a Plinian eruption beginning at approximately 06:00 UTC (McKee et al., 2021), which generated a large umbrella cloud (Horváth et al., 2021). The formation and spread of this cloud was captured by the geostationary satellite Himawari-8. Contours of band 13 (10.4 μm) brightness temperatures, supplied by the Japan Aerospace Exploration Agency's (JAXA) P-Tree System, are used for comparison in this case study, as these most clearly distinguish the umbrella cloud from the plume caused by previous eruptive activity. Only the Plinian phase of the eruption is simulated, as the overall spread of the cloud is dominated by this release.

The initial spread of the Ulawun umbrella cloud was near-axisymmetric. As highlighted in Section 2.4, we expect in this case, the lengthscale L_H to become large so that, over the timescale of the Plinian eruption, particle trajectories remain close to the origin of the dimensionless solution (Figure 1c) where the velocity field tends to an axisymmetric state. We anticipate this will allow the wind-blown parametrization to model near-axisymmetric umbrella cloud growth in this case of strong plume in low wind.

As in the previous case study, Figure 4 shows the modeled ash column loadings for (a) no umbrella cloud, and axisymmetric (b–d) and wind-blown (f–h) parametrizations for the minimum, optimal and maximum fluxes, respectively.

The overestimate of the wind-blown parametrization for the largest volume flux (given by model B), shown in Figure 4h, is larger than that of Webster et al. (2020)'s (Figure 4d). This is due in part to the additional uncertainty in the study of the wind-blown parametrization introduced by variation of the parameter C_D.

As in the Pinatubo case study, there is a peak in column loading along the eastern edge of umbrella clouds generated by Webster et al. (2020)'s axisymmetric parametrization. Though less defined than in the Pinatubo example, this peak illustrates that even small winds are sufficient to cause visible non-physical accumulation in concentrations predicted by axisymmetric parametrizations. In contrast, over the timescale of the eruption, particles remain in the near-axisymmetric region of the wind-blown parametrization's velocity field and there is no accumulation seen in results using this parametrization.

The satellite-observed umbrella cloud outline is centered around the vent, but for all estimates of volume flux, both parametrizations slightly overestimate the easterly extent of the umbrella cloud. This is due to north-westerly wind in the NWP wind field over the height interval occupied by the umbrella cloud (visible in Figure 4a). Better results for both parametrizations can be obtained by reducing the cloud thickness to 1 km and using a modified umbrella cloud height of $H_U = 12$ km, placing the umbrella cloud at altitudes where the NWP wind field is more consistent with the observed spread of the umbrella cloud. These results are provided in Figure S14 in Supporting Information S1, as they require post-hoc adjustment of the parameters and so are not representative of the true predictive ability of the parametrization.

3.5. Calbuco, 2015

The April 2015 eruption of Calbuco volcano in Chile was characterized by two explosive releases of ash, the first between 21:04 UTC and 22:35 UTC on the 22nd and a second sustained release between 03:54 UTC and 10:00 UTC the following day (Van Eaton et al., 2016). The spread of the two resulting umbrella clouds was captured by the GOES-13 satellite, and contours of GOES-13 band 4 (11 μm) brightness data provided by NOAA, as used by Van Eaton et al. (2016) and Webster et al. (2020), are used for comparison in this case study. The two spreading umbrella clouds are distinct and we consider only the second, prolonged, eruption in this study. During the second eruptive phase there was significant vertical wind shear which has proved challenging for simulations using umbrella cloud parametrizations (Mastin & Van Eaton, 2020; Webster et al., 2020). This case study therefore serves to investigate the wind-blown parametrization's capability to produce valid results in these complex meteorological conditions. In this study of Calbuco, NAME runs were computed using the volume flux estimates of Van Eaton et al. (2016), given in Table 1 as models (VE1) and (VE2), as well as each flux computed using the plume models in Section 3.1.

Figure 5 shows the shows the modeled ash column loadings, with panels arranged as in previous case studies. Panels (c) and (g) show median parameter values for the axisymmetric and wind-blown parametrizations, respectively.

Reasonable descriptions of cloud shape are recovered by both parametrizations, though both overestimate the northerly spread, and the wind-blown parametrization overestimates the cloud spread for all but the smallest values of K.

The axisymmetric parametrization predicts a very nonuniform ash column loading. This is in part due to two numerical artifacts in the axisymmetric parametrization previously mentioned, namely moderate accumulation along the downwind edge of the cloud, and a prominent decrease in ash column loading in the center of the eastward traveling component of the cloud, due to numerical error in the time stepping of trajectories. In contrast, the column loading predicted by the wind-blown parametrization is much more uniform over the umbrella cloud.

There is a discrepancy between the dominant north-easterly spread predicted by NAME and the more northerly spread of the real cloud. This was previously observed by Webster et al. (2020), who attributed it to error in either the NWP wind field or observed umbrella cloud height. As Webster et al. (2020) noted, closer agreement between predictions of the wind-blown parametrizations and satellite observations can be obtained by assuming an umbrella cloud height of 19–20 km.

3.6. Operational Use

For the wind-blown parametrization to be suitable for operational use, there must be a clear selection process for model parameters Q, C_D, and N, and the impact of the-blown parametrization on model runtime must be small.

Across the four case studies, no single value of the parameter C_v in Morton et al. (1956)'s 1-D plume model was found to be optimal for determining the volume flux in all case studies. This is consistent with the results of Suzuki and Koyaguchi (2009)'s 3-D numerical simulations of volcanic plumes, in which C_v varies significantly depending on eruption size and atmospheric conditions. The best agreement with observations was found when Q was determined from Morton et al. (1956)'s 1-D plume model, with the chosen value of C_v based on the simulation of Suzuki and Koyaguchi (2009) with the closest total column rise height H_T to that being modeled (model SK). We therefore recommend this approach for selection of Q in operational use.

The wind-blown parametrization has been tested with a wide range of turbulent skin drag values, $C_D \in [0.001, 0.01, 0.1]$, reflecting the range of measured or inferred values in the literature. The relative insensitivity of the model to C_D means that the choice of plume model, determining Q, typically had resulted in greater changes to the model output than a variation of C_D within this range. Across the four case studies in this paper, an intermediate value $C_D = 0.01$—combined with flux determined by SK, and the fixed value $N = 0.02\ s^{-1}$ used throughout this paper—produces good predictions, and at worst moderate overestimates of cloud spread in the challenging wind-shear affected Calbuco case study. The value $C_D = 0.01$ is therefore recommended for operational use, with the proviso that this may not be appropriate for eruption conditions that are very different from the cases studied here. Across the four case studies, the wind-blown parametrization with operational procedure set out above predicts ash column loadings that are generally closer to observations of cloud shape and free of numerical artifacts, compared to predictions from operational procedure and parametrization of Webster et al. (2020) (Supporting Information, Figure S13 in Supporting Information S1).

The time constraints on operational use require that an umbrella cloud parametrization does not drastically increase the runtime of a VATDM. To evaluate the computational cost of the new parametrization on NAME, the runtime of the case studies in this section was measured (Table 2). Parameters were selected according to the operational procedure recommended above for the wind-blown parametrization and as instructed in Webster et al. (2020) for their axisymmetric parametrization. NAME output products and their spatial and temporal resolutions, and a model particle release rate of 15,000 particles/hr, were selected according to the operational procedure at the London VAAC (Witham et al., 2019). Dispersion following each eruption was simulated for 24 hr following the onset of eruption, rounded down to the nearest clock hour.

Webster et al. (2020)'s parametrization results in a minor increase in model runtime across all four case studies. The improved skill of the wind-blown parametrization comes at a greater computational cost, though for the Pinatubo, Ulawun, and Calbuco case studies, the increase in runtime due to the wind-blow parametrization is still a small proportion of the overall run time. The computational cost of the wind-blown parametrization is greatest when the cloud is highly non-axisymmetric, such as at Puyehue, since this cloud geometry results in many particles requiring the most computationally expensive part of the wind-blown parametrization, namely the numerical integration of particle trajectories through the interpolated precalculated umbrella cloud velocity field (Equation 19). The computational cost of umbrella schemes is also proportional to the duration of the run for which the eruption is active, here longest for Puyehue, which was active for the entire 24 hr period. Puyehue therefore represents a worst-case scenario for the computational cost of the wind-blown parametrization. The absolute increase in runtime for a simulation of 24 model hours is nonetheless an increase of less than 2 min, which is likely to be an acceptable trade-off for the significantly greater skill of the wind-blown parametrization for highly non-axisymmetric umbrella clouds of this sort (Figure 2).

4. Discussion

The results of the Puyehue case study (Section 3.2) illustrate an important effect of the interaction of umbrella clouds with wind, namely that buoyancy spreading does not solely act to transport ash radially away from the vent. When the cloud is blown by wind, the buoyancy spreading then acts in the orthogonal direction, spreading the cloud laterally rather than expanding it away from the source. The underprediction of Puyehue plume width by the axisymmetric parametrization (Figures 2b–2d) reflects the omission of this lateral spreading in the axisymmetric parametrization. The results of this case study indicate that buoyancy spreading can have a significant influence on ash dispersal even when a plume is highly wind-blown and does not resemble the circular umbrella cloud archetype—and furthermore that the effect of buoyancy on such plumes is not well described by an axisymmetric umbrella cloud model.

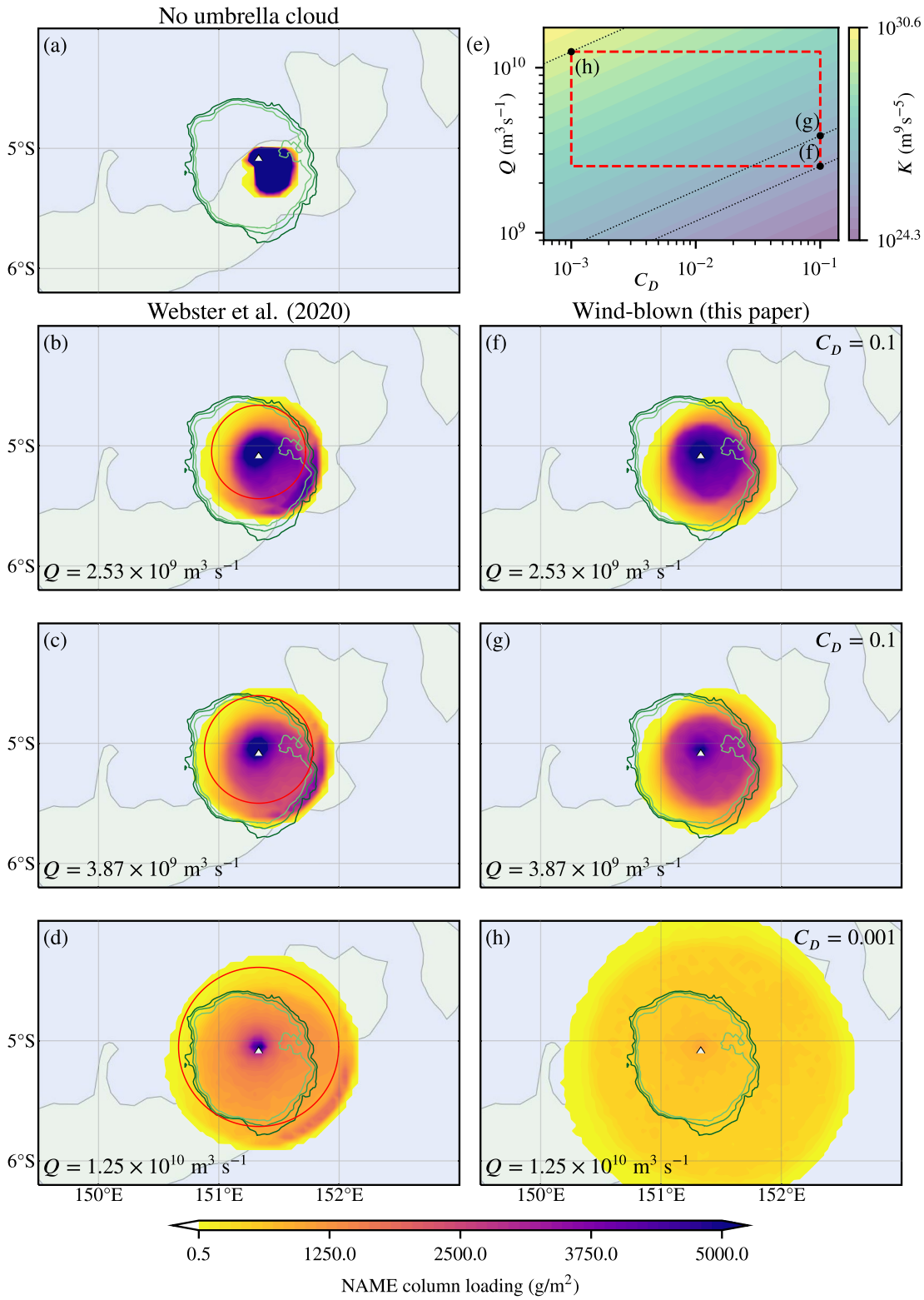

Figure 4. Numerical Atmospheric-dispersion Modeling Environment (NAME) simulations of the Plinian phase of the 2019 Ulawun eruption at 07:10 UTC. Ash column loadings are illustrated by the yellow/purple heatmap, overlaid with green contours of 10.4 μm brightness temperature at 205, 215, and 225K (light to dark). The heatmap boundary corresponds to a loading of 0.5 gm^{-2}. Panel (a) does not use an umbrella parametrization. Panels (b–d) use the axisymmetric parametrization (Equation 11) with volume fluxes predicted by models (D), (SK), and (B), respectively. Red circles in panels (b–d) illustrate the boundary of the umbrella region (Equation 8). Panel (e) maps the parameter space of the wind-blown parametrization. Panels (f–h) use the wind-blown parametrization with volumes fluxes predicted by models (D), (SK), and (B), respectively.

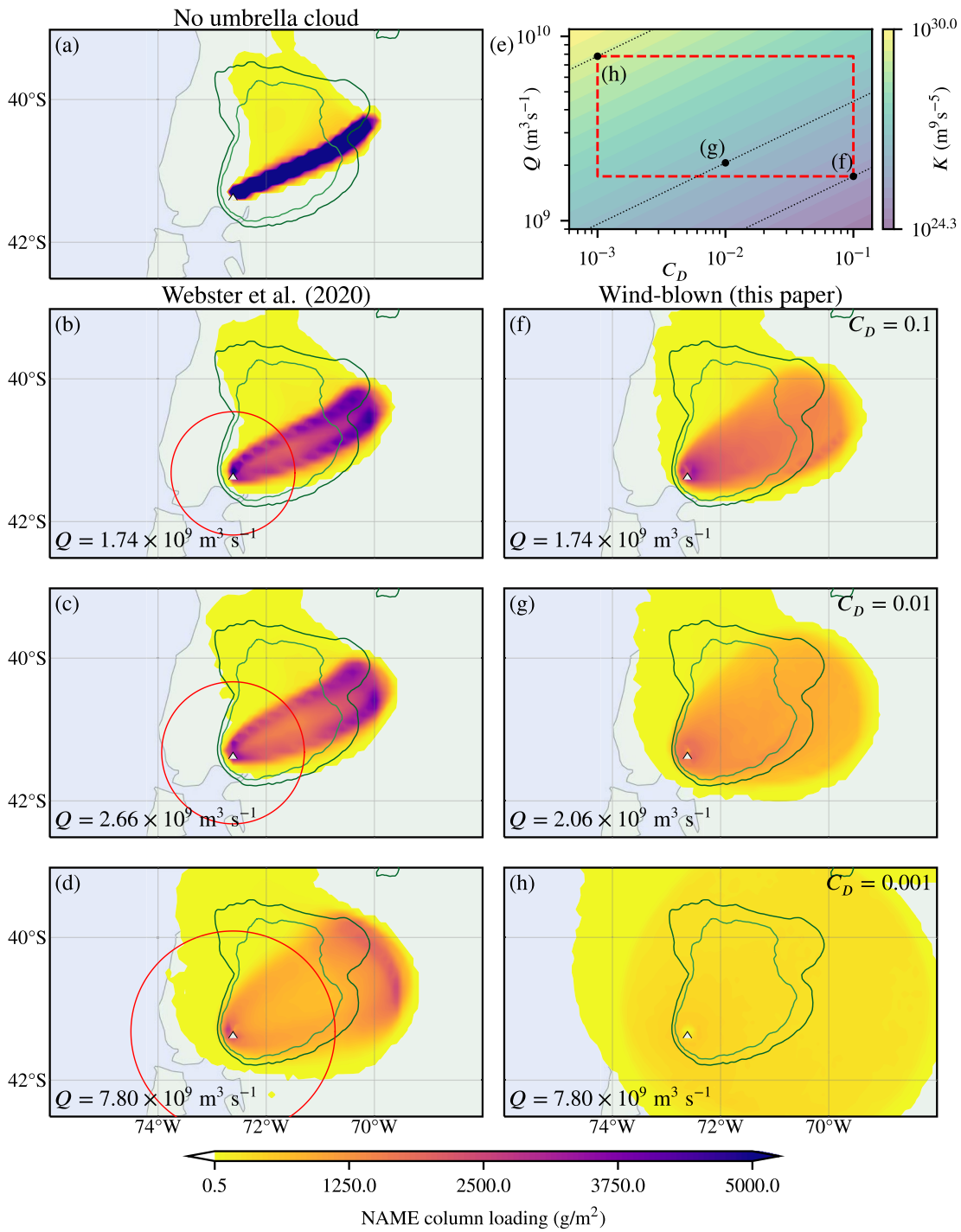

Figure 5. Numerical Atmospheric-dispersion Modeling Environment (NAME) simulations of the second phase of the 2015 Calbuco eruption at 08:37 UTC on 23 April 2015. Ash column loadings are illustrated by the yellow/purple heatmap, overlaid with green contours of 11 μm brightness temperature 225 and 255 K (light to dark). The heatmap boundary corresponds to a loading of 0.5 gm^{-2}. Panel (a) does not use an umbrella parametrization. Panels (c–d) use the axisymmetric parametrization (Equation 11) with volume fluxes predicted by models (D), (SK), and (VE2), respectively. Red circles in panels (b–d) illustrate the boundary of the umbrella region (Equation 8). Panel (e) maps the parameter space of the wind-blown parametrization. Panels (f–h) use the wind-blown parametrization with volumes fluxes predicted by models (D), (BK), and (VE2), respectively.

As illustrated in Figure 1 and in the four case studies, volcanic plumes may form a continuous series of morphologies in which wind and buoyancy play varying roles, ranging from circular umbrella clouds (formed by strong eruptions in light wind) to wind-blown plumes (formed by weaker eruptions in high winds). Most Plinian erup-

Table 2
The Length of Time, in Seconds, Taken to Simulate Dispersion Over a 24 hr Period Following the Eruption Onset Times Given in Table 1

	No umbrella cloud	Axisymmetric	Wind-blown
Puyehue	116.7 s	121.3 s (+4.6 s)	221.3 s (+104.6 s)
Pinatubo	88.5 s	91.2 s (+2.7 s)	97.8 s (+9.3 s)
Ulawun	25.8 s	26.6 s (+0.8 s)	27.2 s (+1.4 s)
Calbuco	74.2 s	75.5 s (+1.3 s)	85.7 s (+11.5 s)

Note. The increase in computation time between simulations with and without umbrella cloud schemes is given in seconds alongside the runtime. Timings measured using NAME 8.1 in serial mode, on a single thread of an AMD 1950X processor.

tions, including all four studied here, lie somewhere between these two endmembers, with both buoyancy spreading and wind having a significant role. In these cases, the nonlinear interaction and two-way coupling between buoyancy and wind can lead to behavior that is not present in either endmember, such as the lateral buoyancy spreading in the Puyehue case study. This emphasizes the importance of including such interactions in the underlying physical equations used for volcanic plume modeling.

The case studies here demonstrate the applicability of the proposed parametrization across a range of wind conditions and eruption fluxes corresponding to sustained Plinian volcanic eruptions (VEI 4–6) where umbrella clouds and buoyant spreading of plumes is significant. We now discuss the applicability and limitations of the parametrization for more general eruption conditions. Smaller eruptions in strong winds produce weak "bent-over" plumes with no upwind spread (Sparks et al., 1997) and negligible effect of buoyancy in the lateral spreading downwind. Correspondingly, as noted previously, the influence of the parametrization presented here on particle transport becomes negligible for small fluxes. In the largest ultra-Plinian eruptions (VEI $\geq$6), the new parametrization approaches the radial buoyancy-dominated spreading that is inferred from ash deposits of historical supereruptions (Mastin et al., 2014). The new parametrization describes umbrella cloud development from a sustained eruption, in which most of the umbrella cloud growth occurs while the eruption is ongoing. In highly unsteady or transient eruptions, substantial umbrella cloud growth may occur after the eruption has ceased, when the umbrella cloud is not significantly increasing in volume but continues to spread laterally as it thins vertically (Pouget et al., 2016). Such dynamics are described by the full shallow-layer model (Johnson et al., 2015; Pouget et al., 2016) but not the simplified parametrization presented here. The assumption of a uniform wind in the derivation of the umbrella cloud parametrization is less well justified for eruptions such as Calbuco 2015, in which significant wind shear occurs across the depth of the umbrella cloud, and the observed umbrella cloud shape is correspondingly less well predicted in this case study.

While there is strong evidence that the non-axisymmetric parametrization improves the description of the horizontal distribution of ash, the wind-blown parametrization presented here, like axisymmetric parametrizations, does not account for the thickness of the cloud: it is assumed that all particles remain within the vertical extent of the umbrella cloud. Vertical displacement of particles due to thinning of the ash cloud with increasing distance from the source is also neglected in both parametrizations, which may result underestimations of ash concentrations (and overestimates of cloud thickness), even when ash column loadings are predicted accurately. Inclusion of this thinning within umbrella cloud parametrizations may be important for applications where predictions of the vertical distribution of ash are required, such as in future use by VAACs (International Civil Aviation Organization, 2021a).

The skill of the wind-blown parametrization in the case studies here further validate the application of the shallow-layer intrusion equations to the buoyancy-driven spread of volcanic ash in the atmosphere. Together with previous work (de' Michieli Vitturi & Pardini, 2021; Pouget et al., 2016), this suggests including additional information from shallow-layer models could improve the predictive capability of umbrella cloud models. In particular, cloud depths determined by shallow-layer solutions could be used to better describe the vertical distribution of ash in umbrella clouds.

5. Conclusion

A new parametrization of wind-blown umbrella cloud spreading, based on the shallow-layer intrusion equations, has been developed and subsequently tested in the Lagrangian ash transport model NAME. The new parametrization typically has only slightly greater computational cost than previous axisymmetric parametrizations, but much better captures the lateral buoyancy-driven spread of wind-blown plumes (Bursik, Carey, & Sparks, 1992; Johnson et al., 2015), such as that of Puyehue 2011, compared to an under-prediction of the plume width by a previous axisymmetric umbrella-cloud parametrization. In eruptions, where wind is less significant and the plume remains roughly circular, the new parametrization predicts similar umbrella cloud shapes to previous models but is much less susceptible to a spurious accumulation of high ash concentrations on the downwind edges of the modeled clouds.

The improved predictions of umbrella cloud extent that we obtain have two major areas of application. The first is in the context of volcanological research, where improved predictions of the umbrella cloud growth may improve the inference of eruption source parameters from volcanic plume observations. Umbrella cloud diameter has been used directly to infer the volume flux at neutral buoyancy level (e.g., Bear-Crozier et al., 2020; Gupta et al., 2022; Hargie et al., 2019; Pouget et al., 2016), most commonly using the scaling law and circular umbrella cloud assumption of Woods and Kienle (1994). The parametrization presented here may improve the accuracy of such inferences, and allow them to be made where the umbrella cloud is significantly wind-affected. Inversion methods that use VATDM predictions to infer eruption source parameters from satellite observations (e.g., Eckhardt et al., 2008; Esse et al., 2024; Kristiansen et al., 2012) may also benefit from the inclusion of umbrella cloud parametrization in the VATDM.

Second, in the operational context, the parametrization presented here may increase the accuracy of plume dispersal forecasts, where underestimation of the extent of the dispersed ash is a particular concern. As demonstrated by the case study of Puyehue 2011, buoyancy-driven spreading is not limited to circular umbrella clouds, but can be significant even when the plume is predominantly blown downwind, requiring a model such as the one presented here in which the interaction between umbrella cloud and ambient wind is captured, to avoid underestimation of plume width. As requirements on VAACs move from reporting simply the region in which ash may be present, to providing much more detailed information on the vertical and horizontal variation of ash concentration (International Civil Aviation Organization, 2021a), it is becoming increasingly important that the buoyancy-driven spreading processes modeled here are included in the VATDMs used for operational ash forecasting.

Appendix A: Asymptotic Behavior of the Non-Axisymmetric Parametrization

A feature of the non-axisymmetric parametrization stated in Section 2.3 is that the behavior of the full solution to Equation 1 is recovered in both the near source ($r \ll 1$) and far downstream ($x \gg 1$) regions. The proof of these results are given in this appendix.

A1. Near-Source Region

Close to the source, Johnson et al. (2015) determined that an intrusion spreading in a stationary atmosphere subject to the full governing Equation 1 has depth and velocity given by

$$h^\star = \left(\frac{5}{\pi^2}\right)^{1/5} r^{\star\,-1/5} \text{ and } u_r^\star = \frac{1}{2}\left(5\pi^3\right)^{-1/5} r^{\star\,-4/5}, \tag{A1}$$

when expressed in variables non-dimensionalized by Equation 16.

Here, we show that as $r^\star \ll 1$, the behavior of the simplified system (Equation 20) tends precisely to Equation A1. To study the solution near the source, we introduce the rescaled coordinate $r^\star = \xi R^\star$, supposing that $\xi^\star \ll 1$ and $R^\star = O(1)$. Further, suppose $h^\star = \xi^{-1/5} H_0^\star + \xi^{3/5} H_1^\star + \ldots$. Introducing the operator

$$\nabla_R^\star = \left(\frac{\partial}{\partial R^\star}, \frac{\partial}{\partial \theta}\right), \tag{A2}$$

We find that to leading order in ξ, Equation 20 is equivalent to

$$\nabla_R^\star \cdot \left(\frac{H_0^{\star\,2} \nabla_R^\star H_0^\star}{2\sqrt{\left|\nabla_R^\star H_0^\star\right|}}\right) = 0. \tag{A3}$$

Equation A3 has solution $H_0^\star = k_0 R^{\star\,-1/5}$, where k_0 is a constant to be determined. Considering the next order terms, we have

$$\varepsilon^{-1}\nabla_R^\star\cdot\left(\left(\varepsilon^{-1/5}H_0^\star+\varepsilon^{3/5}H_1^\star\right)\boldsymbol{e}_x-\frac{\varepsilon^{-1}H_0^{\star 2}\nabla_R^\star H_0^\star+\varepsilon^{-1/5}\left(2H_0^\star H_1^\star\nabla_R^\star H_0^\star+H_0^{\star 2}\nabla_R^\star H_1^\star\right)}{2\sqrt{\left|\nabla_R^\star H_0^\star\right|}}+\varepsilon^{-1/5}\frac{H_0^{\star 2}\nabla_R^\star H_0^\star\left(\nabla_R^\star H_0^\star\cdot\nabla_R^\star H_1^\star\right)}{4\left|\nabla_R^\star H_0^\star\right|^{5/2}}\right)=0. \tag{A4}$$

On substitution of the leading order solution, $H_0^\star=k_0R^{\star -1/5}$, we have

$$\nabla_R^\star\left(k_0R^{\star -1/5}(\cos\theta\boldsymbol{e}_r-\sin\theta\boldsymbol{e}_\theta)+k_0^{3/2}\left(\frac{1}{\sqrt{5}}R^{\star -4/5}H_1^\star\boldsymbol{e}_r-\frac{\sqrt{5}}{2}R^{\star 1/5}\nabla_R^\star H_1^\star+\frac{\sqrt{5}}{4}R^{\star 1/5}\frac{\partial H_1^\star}{\partial R^\star}\boldsymbol{e}_r\right)\right)=0. \tag{A5}$$

which has solution

$$H_1^\star=\frac{2\sqrt{5}}{27k_0^{1/2}}R^{\star 3/5}\cos\theta. \tag{A6}$$

which gives us the first two terms of the asymptotic expansion for near source depth.

Using Equation 19 and the first two terms in the asymptotic expansion for near source depth, we can recover the velocity field up to and including $O(1)$ terms in ε

$$u_r^\star=\varepsilon^{-4/5}\frac{k_0^{3/2}}{2\sqrt{5}R^{\star 4/5}}+\frac{53}{54}\cos\theta+\cdots,\quad u_\theta^\star=-\frac{22}{27}\sin\theta+\cdots. \tag{A7}$$

We can now determine k_0 using the integral conservation of mass condition

$$\int_0^{2\pi}h^\star u_r^\star\mathrm{d}\theta=\frac{1}{r^\star}. \tag{A8}$$

To leading order in ε this condition is

$$\int_0^{2\pi}\frac{k_0^{5/2}}{2r^\star\sqrt{5}}\mathrm{d}\theta=\frac{1}{r^\star}, \tag{A9}$$

from which we obtain $k_0=\left(5/\pi^2\right)^{1/5}$, confirming that we obtain precisely (Equation A1) for $r^\star\ll 1$.

A2. Downstream Region

Far downstream, Johnson et al. (2015) determined that as the ratio of crosswind to downwind velocities $\epsilon=|v/u|$ (and consequently the ratio of crosswind to downwind lengthscales) becomes asymptotically small, $\epsilon\ll 1$, the solution to the full shallow-layer system (Equation 1) tends to

$$u^\star=1,\ v^\star=\frac{y^\star}{3x^\star},\ h^\star=\frac{\hat{C}}{(2\pi)^{1/2}x^{\star 1/3}}\left(\frac{2}{3}\right)^{2/3}\left(1-\left(\frac{y^\star}{w^\star(x^\star)}\right)^3\right)^{1/3}, \tag{A10}$$

where

$$w^\star\left(x^\star\right)=\frac{\hat{C}}{(2\pi)^{1/2}}x^{\star 1/3}\text{ and }\hat{C}=2.159\ldots, \tag{A11}$$

to leading order in ϵ, when expressed in variables non-dimensionalized by Equation 16. Here, we show that as downwind lengthscales become much larger than crosswind lengthscales, the solution of simplified system (Equation 20) is precisely (Equation A10). That is, both solutions have the same behavior far downstream.

We introduce the downstream coordinates and variables

$$X^\star = \varepsilon x^\star, \quad Y^\star = \varepsilon^{1/3} y^\star \quad \text{and} \quad H^\star = \varepsilon^{-1/3} h^\star, \tag{A12}$$

expressed in terms of the ordering parameter $\varepsilon = |y^\star / x^\star|^{3/2}$, which is assumed to be small. Downstream quantities $X^\star$, $Y^\star$, and $H^\star$ are all $O(1)$. To leading order in ε, the governing Equation 20 is

$$\varepsilon^{4/3} \frac{\partial H^\star}{\partial X^\star} - \varepsilon^{4/3} \frac{\partial}{\partial Y^\star} \left(\frac{H^{\star 2} \frac{\partial H^\star}{\partial Y^\star}}{2\sqrt{\left| \frac{\partial H^\star}{\partial Y^\star} \right|}} \right) + O\left(\varepsilon^{8/3}\right) = 0, \tag{A13}$$

since

$$\sqrt{|\nabla^\star h^\star|} = \varepsilon^{1/3} \sqrt{\left| \frac{\partial H^\star}{\partial Y^\star} \right|} + O\left(\varepsilon^{2/3}\right). \tag{A14}$$

Given the problem is symmetric about $Y^\star = 0$, we can restrict our attention to the upper half plane $Y^\star \geq 0$. Further, we make the assumption that $H^\star(X^\star, Y^\star)$ is monotonically decreasing in $Y^\star$ in this region. Equation A13 then reduces to

$$\frac{\partial H^\star}{\partial X^\star} + \frac{\partial}{\partial Y^\star} \left(\frac{H^{\star 2}}{2} \left(-\frac{\partial H^\star}{\partial Y^\star} \right)^{1/2} \right) = 0, \tag{A15}$$

to leading order in ε. Introducing the similarity variables

$$\zeta^\star = \frac{Y^\star}{C X^{\star 1/3}} \quad \text{and} \quad H^\star = C X^{\star -1/3} \mathcal{H}^\star\left(\zeta^\star\right), \tag{A16}$$

where C is a constant to be determined, Equation A15 is then equivalent to the second order ODE in $\zeta^\star$

$$\frac{\mathrm{d}}{\mathrm{d}\zeta^\star} \left(\frac{\mathcal{H}^{\star 2}}{2} \left(\frac{\mathrm{d}\mathcal{H}^\star}{\mathrm{d}\zeta^\star} \right)^{1/2} - \frac{1}{3} \zeta^\star \mathcal{H}^\star \right) = 0, \tag{A17}$$

to be solved subject to the boundary conditions

$$\mathcal{H}^\star\left(\zeta^\star = 1\right) = 0, \text{ and } \mathcal{H}^{\star\prime}\left(\zeta^\star = 0\right) = 0. \tag{A18}$$

The conditions (Equation A18) arise from the simplified boundary condition $h = 0$ applied at the flow front and the symmetry of the solution about $Y = 0$ respectively. Integrating (Equation A17) and applying the gradient boundary condition in Equation A18 we have

$$\frac{\mathrm{d}\mathcal{H}^\star}{\mathrm{d}\zeta^\star} = -\frac{4\zeta^{\star 2}}{9\mathcal{H}^{\star 2}}. \tag{A19}$$

Now integrating (Equation A19) and applying the zero-depth boundary condition in Equation A18, we find the solution

$$\mathcal{H}^\star = \left(\frac{2}{3}\right)^{2/3} \left(1 - \zeta^{\star 3}\right)^{\frac{1}{3}}. \tag{A20}$$

This implies

$$H^\star = C X^{\star -1/3} \left(\frac{2}{3}\right)^{2/3} \left(1 - \left(\frac{Y^\star}{C X^{\star 1/3}} \right)^3 \right)^{\frac{1}{3}}. \tag{A21}$$

Coupled with Equation 19, this implies that, to leading order in ε,

$$u^\star = 1, \quad v^\star = \frac{y^\star}{3x^\star}, \quad w^\star = C x^{\star 1/3}, \tag{A22}$$

where $w^\star$ is the half-width of the intrusion. The constant C is determined by global conservation of mass;

$$\int_0^{Cx^{\star\,1/3}} h^\star u^\star \mathrm{d}y^\star = \frac{1}{2}, \tag{A23}$$

from which we determine $C = \hat{C}/(2\pi)^{1/2}$, such that Equations A21 and A22 coincide exactly with the work of Johnson et al. (2015). This confirms our claim that the simplified system (Equation 20) has the same behavior downstream as that of the full system.

A3. Trajectories in the Asymptotic Limits $r \ll 1$ and $x \gg 1$

In theory, the method set out in Section 2.4 allows the length and timescales (Equation 16) to take any value between zero and infinity. This makes choosing a grid for the numerical solution to Equation 20 difficult, given that we wish to avoid recomputing the solution at runtime. This is resolved by using asymptotic trajectories both near the origin and far downstream.

In the scheme, particles are released at the origin, $r^\star = 0$. To compute an increment here we use only the leading order term of velocity field (Equation A7). This gives a radial increment,

$$\boldsymbol{d}_w^{0\,\star}\left(\mathbf{0}, \Delta t^\star\right) = \left(\frac{9k_0^{3/2}}{10\sqrt{5}}\Delta t^\star\right)^{5/9}\boldsymbol{e}_r \tag{A24}$$

Away from the origin but near the source, $r^\star < r_E^\star$ (we use $r_E^\star \approx 0.030$, though in general, it should be as small as possible while ensuring computation time remains reasonable), we use an adaptive time step fifth order Runge-Kutta scheme and all terms of the velocity field (Equation A7).

Far downstream, $x^\star > x_D^\star$ (We use $x_D^\star \approx 4.5$, though again in general, this should be as large as possible while ensuring computation time remains reasonable), we use analytic solutions of the leading order velocity field (Equation A22) to compute the increment,

$$\boldsymbol{d}_w^{D\star}\left(\boldsymbol{x}^\star\left(t_n^\star\right), \Delta t^\star\right) = \Delta t^\star \boldsymbol{e}_x + y^\star\left(t_n^\star\right)\left(\left(1 + \frac{\Delta t^\star}{x^\star\left(t_n^\star\right)}\right)^{1/3} - 1\right)\boldsymbol{e}_y. \tag{A25}$$

Data Availability Statement

Satellite measurements used in this research are available in a public repository (Millward et al., 2023), except those from Ulawun, which are available from P-Tree System, Japan Aerospace Exploration Agency (JAXA) at https://www.eorc.jaxa.jp/ptree/. The dimensionless velocity field that underlies the wind-blown parametrization, the NAME input files, and the resulting model outputs used to generate the figures in this paper are also provided in this repository. The NAME 8.1 software (Jones et al., 2007) used to test the wind-blown parametrization may be licensed from the Met Office (https://www.metoffice.gov.uk/, atmospheric.dispersion@metoffice.gov.uk). The Python package iris (Met Office, 2016) was used to load and process NAME outputs, and iris, cartopy (Elson et al., 2020) and matplotlib (Caswell et al., 2021) were used for plotting.

Acknowledgments
C.G.J. is supported by a NERC Highlight Topics grant "V-Plus" NE/S004106/1 and F.J.M. by an EPSRC Studentship EP/R513131/1. The use of imagery from the NASA Worldview application (https://worldview.earthdata.nasa.gov), part of the NASA Earth Observing System Data and Information System (EOSDIS) for the Puyehue case study is acknowledged. Brightness temperature data (produced from Himawari-8) used for the Ulawun case study was supplied by the P-Tree System, Japan Aerospace Exploration Agency (JAXA). The paper benefited from helpful discussions with several members of the V-Plus project and the Met Office Atmospheric Dispersion and Air Quality group, including Mike Burton, Claire Witham, Anja Schmidt, and Hans De Leeuw.

References

Abraham, G., Karelse, M., & Van Os, A. G. (1979). On the magnitude of interfacial shear of subcritical stratified flows in relation with interfacial stability. *Journal of Hydraulic Research*, *17*(4), 273–287. https://doi.org/10.1080/00221687909499572

Baines, P. G. (2013). The dynamics of intrusions into a density-stratified crossflow. *Physics of Fluids*, *25*(7), 076601. https://doi.org/10.1063/1.4811850

Bear-Crozier, A., Pouget, S., Bursik, M., Jansons, E., Denman, J., Tupper, A., & Rustowicz, R. (2020). Automated detection and measurement of volcanic cloud growth: Towards a robust estimate of mass flux, mass loading and eruption duration. *Natural Hazards*, *101*(1), 1–38. https://doi.org/10.1007/s11069-019-03847-2

Beckett, F. M., Witham, C. S., Leadbetter, S. J., Crocker, R., Webster, H. N., Hort, M. C., et al. (2020). Atmospheric dispersion modelling at the London VAAC: A review of developments since the 2010 Eyjafjallajökull volcano ash cloud. *Atmosphere*, *11*(4), 352. https://doi.org/10.3390/atmos11040352

Bloomfield, L. J., & Kerr, R. C. (2000). A theoretical model of a turbulent fountain. *Journal of Fluid Mechanics*, *424*, 197–216. https://doi.org/10.1017/S0022112000001907

Bonadonna, C., Phillips, J. C., & Houghton, B. F. (2005). Modeling tephra sedimentation from a Ruapehu weak plume eruption. *Journal of Geophysical Research: Solid Earth*, *110*(B8), B08209. https://doi.org/10.1029/2004JB003515

Bursik, M. I., Carey, S. N., & Sparks, R. S. J. (1992). A gravity current model for the May 18, 1980 Mount St. Helens plume. *Geophysical Research Letters*, *19*(16), 1663–1666. https://doi.org/10.1029/92GL01639

Bursik, M. I., Sparks, R. S. J., Gilbert, J. S., & Carey, S. N. (1992). Sedimentation of tephra by volcanic plumes: I. Theory and its comparison with a study of the Fogo A Plinian deposit, Sao Miguel (Azores). *Bulletin of Volcanology.*, *54*(4), 329–344. https://doi.org/10.1007/BF00301486

Caswell, T. A., Droettboom, M., Lee, A., de Andrade, E. S., Hunter, J., Firing, E., & Ivanov, P. (2021). matplotlib/matplotlib: REL: v3.3.4 [Software]. https://doi.org/10.5281/zenodo.4475376

Clarkson, R. J., Majewicz, E. J. E., & Mack, P. (2016). A re-evaluation of the 2010 quantitative understanding of the effects volcanic ash has on gas turbine engines. *Proceedings of the Institution of Mechanical Engineers—Part G: Journal of Aerospace Engineering*, *230*(12), 2274–2291. https://doi.org/10.1177/0954410015623372

Collini, E., Osores, M. S., Folch, A., Viramonte, J. G., Villarosa, G., & Salmuni, G. (2013). Volcanic ash forecast during the June 2011 Cordón Caulle eruption. *Natural Hazards*, *66*(2), 389–412. https://doi.org/10.1007/s11069-012-0492-y

Costa, A., Folch, A., & Macedonio, G. (2013). Density-driven transport in the umbrella region of volcanic clouds: Implications for tephra dispersion models. *Geophysical Research Letters*, *40*(18), 4823–4827. https://doi.org/10.1002/grl.50942

de' Michieli Vitturi, M., & Pardini, F. (2021). PLUME-MoM-TSM 1.0.0: A volcanic column and umbrella cloud spreading model. *Geoscientific Model Development*, *14*(3), 1345–1377. https://doi.org/10.5194/gmd-14-1345-2021

Devenish, B. J., Rooney, G. G., & Thomson, D. J. (2010). Large-eddy simulation of a buoyant plume in uniform and stably stratified environments. *Journal of Fluid Mechanics*, *652*, 75–103. https://doi.org/10.1017/S0022112010000017

Eckhardt, S., Prata, A. J., Seibert, P., Stebel, K., & Stohl, A. (2008). Estimation of the vertical profile of sulfur dioxide injection into the atmosphere by a volcanic eruption using satellite column measurements and inverse transport modeling. *Atmospheric Chemistry and Physics*, *8*(14), 3881–3897. https://doi.org/10.5194/acp-8-3881-2008

Elson, P., de Andrade, E. S., Hattersley, R., Campbell, E., May, R., Dawson, A., et al. (2020). SciTools/cartopy: Cartopy 0.18.0[Software]. https://doi.org/10.5281/zenodo.3783894

Esse, B., Burton, M., Hayer, C., Contreras-Arratia, R., Christopher, T., Joseph, E. P., et al. (2024). SO_2 emissions during the 2021 eruption of La Soufrière, St Vincent, revealed with back-trajectory analysis of TROPOMI imagery. *Geological Society, London, Special Publications*, *539*(1), SP539-2022–77. https://doi.org/10.1144/SP539-2022-77

Folch, A., Mingari, L., Gutierrez, N., Hanzich, M., Macedonio, G., & Costa, A. (2020). FALL3D-8.0: A computational model for atmospheric transport and deposition of particles, aerosols and radionuclides—Part 1: Model physics and numerics. *Geoscientific Model Development*, *13*(3), 1431–1458. https://doi.org/10.5194/gmd-13-1431-2020

Folch, A., Mingari, L., & Prata, A. T. (2022). Ensemble-based forecast of volcanic clouds using FALL3D-8.1. *Frontiers in Earth Science*, *9*. https://doi.org/10.3389/feart.2021.741841

Global Volcanism Program. (1991). Report on Pinatubo (Philippines). *Bulletin of the Global Volcanism Network*, *16*(6). https://doi.org/10.5479/si.GVP.BGVN199106-273083

Global Volcanism Program. (2012). Report on Puyehue-Cordon Caulle (Chile). *Bulletin of the Global Volcanism Network*, *37*(3). https://doi.org/10.5479/si.GVP.BGVN201203-357150

Global Volcanism Program. (2015). Report on Calbuco (Chile). *Bulletin of the Global Volcanism Network*, *40*(6). https://doi.org/10.5479/si.GVP.BGVN201506-358020

Global Volcanism Program. (2019). Report on Ulawun (Papua New Guinea). *Bulletin of the Global Volcanism Network*, *44*(9). https://doi.org/10.5479/si.GVP.BGVN201909-252120

Gupta, A. K., Bennartz, R., Fauria, K. E., & Mittal, T. (2022). Eruption chronology of the December 2021 to January 2022 Hunga Tonga-Hunga Ha'apai eruption sequence. *Communications Earth & Environment*, *3*(11), 1–10. https://doi.org/10.1038/s43247-022-00606-3

Hargie, K. A., Van Eaton, A. R., Mastin, L. G., Holzworth, R. H., Ewert, J. W., & Pavolonis, M. (2019). Globally detected volcanic lightning and umbrella dynamics during the 2014 eruption of Kelud, Indonesia. *Journal of Volcanology and Geothermal Research*, *382*, 81–91. https://doi.org/10.1016/j.jvolgeores.2018.10.016

Holasek, R. E., Self, S., & Woods, A. W. (1996). Satellite observations and interpretation of the 1991 Mount Pinatubo eruption plumes. *Journal of Geophysical Research: Solid Earth*, *101*(B12), 27635–27655. https://doi.org/10.1029/96JB01179

Horváth, A., Girina, O. A., Carr, J. L., Wu, D. L., Bril, A. A., Mazurov, A. A., et al. (2021). Geometric estimation of volcanic eruption column height from GOES-R near-limb imagery—Part 2: Case studies. *Atmospheric Chemistry and Physics*, *21*(16), 12207–12226. https://doi.org/10.5194/acp-21-12207-2021

International Civil Aviation Organization. (2017). Fifth Meeting of the Working Group of the Meteorology Panel Meteorological Operations Group (METP WG-MOG/5)—Work Stream 3: International Airways Volcano Watch (IAVW). Retrieved from https://www.icao.int/airnavigation/METP/MOG%20Meeting%20Reports/MOG5-IAVW_Report_V_1_1%20(4).pdf

International Civil Aviation Organization. (2021a). Roadmap for International Airways Volcano Watch (IAVW) in Support of International Air Navigation. Retrieved from https://www.icao.int/airnavigation/METP/MOGVA%20Reference%20Documents/IAVW%20Roadmap%20vs%205.0%20-%2001nov2021.pdf

International Civil Aviation Organization. (2021b). Volcanic ash contingency plan —EUR and NAT regions. Retrieved from https://www.icao.int/EURNAT/EUR%20and%20NAT%20Documents/EUR+NAT%20VACP%20v2.0.1-Corrigendum.pdf

Jay, J., Costa, F., Pritchard, M., Lara, L., Singer, B., & Herrin, J. (2014). Locating magma reservoirs using InSAR and petrology before and during the 2011–2012 Cordón Caulle silicic eruption. *Earth and Planetary Science Letters*, *395*, 254–266. https://doi.org/10.1016/j.epsl.2014.03.046

Johnson, C. G., Hogg, A. J., Huppert, H. E., Sparks, R. J. R., Phillips, J. C., Slim, A. C., & Woodhouse, M. J. (2015). Modelling intrusions through quiescent and moving ambients. *Journal of Fluid Mechanics*, *771*, 370–406. https://doi.org/10.1017/jfm.2015.180

Jones, A., Thomson, D., Hort, M., & Devenish, B. (2007). The U.K. Met Office's next-generation atmospheric dispersion model, NAME III. In C. Borrego, & A. Norman (Eds.), *Air pollution modeling and its application XVII* (pp. 580–589). Springer US. https://doi.org/10.1007/978-0-387-68854-1_62

Kristiansen, N. I., Stohl, A., Prata, A. J., Bukowiecki, N., Dacre, H., Eckhardt, S., et al. (2012). Performance assessment of a volcanic ash transport model mini-ensemble used for inverse modeling of the 2010 Eyjafjallajökull eruption. *Journal of Geophysical Research*, *117*(D20), D00U11. https://doi.org/10.1029/2011JD016844

Kurganov, A., & Tadmor, E. (2000). New high-resolution central schemes for nonlinear conservation laws and convection—Diffusion equations. *Journal of Computational Physics*, *160*(1), 241–282. https://doi.org/10.1006/jcph.2000.6459

Lynch, J. S., & Stephens, G. (1996). Mount Pinatubo: A satellite perspective of the June 1991 eruptions. In C. S. Newhall, & R. S. Punongbayan (Eds.), *Fire and mud: Eruptions and Lahars of Mount Pinatubo, Philippines*. University of Washington Press.

Mastin, L. G. (2014). Testing the accuracy of a 1-D volcanic plume model in estimating mass eruption rate. *Journal of Geophysical Research: Atmospheres*, *119*(5), 2474–2495. https://doi.org/10.1002/2013JD020604

Mastin, L. G., & Van Eaton, A. R. (2020). Comparing simulations of umbrella-cloud growth and ash transport with observations from Pinatubo, Kelud, and Calbuco volcanoes. *Atmosphere*, *11*(10), 1038. https://doi.org/10.3390/atmos11101038

Mastin, L. G., Van Eaton, A. R., & Lowenstern, J. B. (2014). Modeling ash fall distribution from a Yellowstone supereruption. *Geochemistry, Geophysics, Geosystems*, *15*(8), 3459–3475. https://doi.org/10.1002/2014GC005469

McKee, K., Smith, C. M., Reath, K., Snee, E., Maher, S., Matoza, R. S., et al. (2021). Evaluating the state-of-the-art in remote volcanic eruption characterization—Part II: Ulawun volcano, Papua New Guinea. *Journal of Volcanology and Geothermal Research*, *420*, 107381. https://doi.org/10.1016/j.jvolgeores.2021.107381

Met Office. (2016). Iris v1.9.2 [Software]. https://doi.org/10.5281/zenodo.51860

Millward, F. J., Webster, H. N., & Johnson, C. G. (2023). Data for "Modelling Wind-blown Umbrella Clouds in Lagrangian Dispersion Models". [Dataset]. https://doi.org/10.48420/22656460

Morton, B. R., Taylor, G. I., & Turner, J. S. (1956). Turbulent gravitational convection from maintained and instantaneous sources. *Proceedings of the Royal Society of London. Series A. Mathematical and Physical Sciences*, *234*(1196), 1–23. https://doi.org/10.1098/rspa.1956.0011

Newhall, C. G., & Self, S. (1982). The volcanic explosivity index (VEI) an estimate of explosive magnitude for historical volcanism. *Journal of Geophysical Research: Oceans*, *87*(C2), 1231–1238. https://doi.org/10.1029/JC087iC02p01231

Pouget, S., Bursik, M., Johnson, C. G., Hogg, A. J., Phillips, J. C., & Sparks, R. S. J. (2016). Interpretation of umbrella cloud growth and morphology: Implications for flow regimes of short-lived and long-lived eruptions. *Bulletin of Volcanology*, *78*(1), 1. https://doi.org/10.1007/s00445-015-0993-0

Prata, A. T., Mingari, L., Folch, A., Macedonio, G., & Costa, A. (2021). FALL3D-8.0: A computational model for atmospheric transport and deposition of particles, aerosols and radionuclides—Part 2: Model validation. *Geoscientific Model Development*, *14*(1), 409–436. https://doi.org/10.5194/gmd-14-409-2021

Rooney, G. G., & Devenish, B. J. (2014). Plume rise and spread in a linearly stratified environment. *Geophysical & Astrophysical Fluid Dynamics*, *108*(2), 168–190. https://doi.org/10.1080/03091929.2013.849345

Schwaiger, H. F., Denlinger, R. P., & Mastin, L. G. (2012). Ash3d: A finite-volume, conservative numerical model for ash transport and tephra deposition. *Journal of Geophysical Research: Solid Earth*, *117*(B4). https://doi.org/10.1029/2011JB008968

Sparks, R. S. J. (1986). The dimensions and dynamics of volcanic eruption columns. *Bulletin of Volcanology*, *48*(1), 3–15. https://doi.org/10.1007/BF01073509

Sparks, R. S. J., Bursik, M. I., Carey, S. N., Gilbert, J. S., Glaze, L. S., Sigurdsson, H., & Woods, A. W. (1997). *Volcanic plumes*. Wiley.

Suzuki, Y. J., & Koyaguchi, T. (2009). A three-dimensional numerical simulation of spreading umbrella clouds. *Journal of Geophysical Research: Solid Earth*, *114*(B3), B03209. https://doi.org/10.1029/2007JB005369

Ungarish, M. (2009). *An introduction to gravity currents and intrusions*. CRC Press. https://doi.org/10.1201/9781584889045

Ungarish, M., & Huppert, H. E. (2002). On gravity currents propagating at the base of a stratified ambient. *Journal of Fluid Mechanics*, *458*, 283–301. https://doi.org/10.1017/S0022112002007978

Van Eaton, A. R., Amigo, A., Bertin, D., Mastin, L. G., Giacosa, R. E., González, J., et al. (2016). Volcanic lightning and plume behavior reveal evolving hazards during the April 2015 eruption of Calbuco volcano, Chile. *Geophysical Research Letters*, *43*(7), 3563–3571. https://doi.org/10.1002/2016GL068076

Vidal, L., Nesbitt, S. W., Salio, P., Farias, C., Nicora, M. G., Osores, M. S., et al. (2017). C-band dual-polarization radar observations of a massive volcanic eruption in south America. *Ieee Journal of Selected Topics in Applied Earth Observations and Remote Sensing*, *10*(3), 960–974. https://doi.org/10.1109/JSTARS.2016.2640227

Webster, H. N., Devenish, B. J., Mastin, L. G., Thomson, D. J., & Van Eaton, A. R. (2020). Operational modelling of umbrella cloud growth in a Lagrangian volcanic ash transport and dispersion model. *Atmosphere*, *11*(2), 200. https://doi.org/10.3390/atmos11020200

Webster, H. N., Thomson, D. J., Johnson, B. T., Heard, I. P. C., Turnbull, K., Marenco, F., et al. (2012). Operational prediction of ash concentrations in the distal volcanic cloud from the 2010 Eyjafjallajökull eruption. *Journal of Geophysical Research: Atmospheres*, *117*(D20). https://doi.org/10.1029/2011JD016790

Witham, C., Hort, M., Thomson, D., Devenish, B., Webster, H., & Beckett, F. (2019). The current volcanic ash modelling set-up at the London VAAC (Met Office Technical Summary (v1.6)). *Met Office*.

Witham, C., Webster, H., Hort, M., Jones, A., & Thomson, D. (2012). Modelling concentrations of volcanic ash encountered by aircraft in past eruptions. *Atmospheric Environment*, *48*, 219–229. https://doi.org/10.1016/j.atmosenv.2011.06.073

Woods, A. W. (1988). The fluid dynamics and thermodynamics of eruption columns. *Bulletin of Volcanology*, *50*(3), 169–193. https://doi.org/10.1007/BF01079681

Woods, A. W., & Kienle, J. (1994). The dynamics and thermodynamics of volcanic clouds: Theory and observations from the April 15 and April 21, 1990 eruptions of Redoubt Volcano, Alaska. *Journal of Volcanology and Geothermal Research*, *62*(1), 273–299. https://doi.org/10.1016/0377-0273(94)90037-X